JOURNAL OF MATERIALS SCIENCE 23 (1988) 4181–4208

Review
Metallurgical applications of secondary ion mass spectrometry (SIMS)

F. DEGRÈVE, N. A. THORNE, J. M. LANG
Péchiney, Centre de Recherches de Voreppe, BP27, 38340 Voreppe, France

This paper reviews the unique advantages provided by secondary ion mass spectrometry (SIMS) for the chemical characterization of heterogeneous materials, with particular attention paid to the field of materials science: detection and imaging of the lateral distribution of every element from hydrogen to uranium, even at very low concentration and excellent depth resolution in the nanometre range. The advantages brought by coupling SIMS with other conventional (SEM, electron probe microanalysis, TEM/SEM) and new (X-ray photoelectron spectroscopy, nuclear microprobe) microscopical and microanalytical techniques are mainly illustrated by examples taken from the author's laboratory (essentially in the field of aluminium metallurgy): quantitative analysis of the solid solution and within phases, surface, thin film and interface analysis by depth profiles. Special attention will be focused on the advantages of SIMS as an "analytical microscope" and the importance of high mass resolution to solve practical problems. The difficulties of quantification associated with the variations of sputtering rate of materials and ionization probability of the emitted ionic species in multiphase systems will also be discussed.

Contents

1. Introduction
2. Principles of SIMS
   2.1. Mass spectrometry
   2.2. Primary beam
   2.3. Ion-solid interaction
   2.4. Lateral distribution of atomic and molecular species by ion micrography
   2.5. In-depth analysis
   2.6. Quantitative analysis
3. Qualitative analysis of metallurgical samples by mass spectra
   3.1. Panoramic elemental analysis at low mass resolution
   3.2. Chemical state information by molecular ions
   3.3. Accurate analysis at high mass resolution
4. Qualitative microscopy by ion imaging
   4.1. Elemental ion microscopy
   4.2. Intermetallic and molecular ion microscopy
5. Quantitative analysis in the bulk of metallurgical samples
   5.1. In the matrix
      5.1.1. Elements at high concentration within the matrix
      5.1.2. Elements at low concentration within the matrix
   5.2. Phases, small precipitates
6. Surface, thin films and interface analysis by depth profiles
   6.1. Parallel interface(s)
      6.1.1. Thin oxide layers
      6.1.2. Multilayered films
      6.1.3. Bulk diffusion
      6.1.4. Organic thin films on metallic substrates
   6.2. Randomly oriented interface(s)
      6.2.1. Concentration profile at a matrix–precipitate interface
      6.2.2. Segregation at grain boundaries
      6.2.3. Enrichment at a matrix–fibre interface in a composite material
7. Use of isotopic tracers for mechanism studies
8. Conclusion

1. Introduction

One important objective in materials science consists in relating the macroscopic properties of materials to their microscopic characteristics. In the field of materials science, samples are by nature heterogeneous on both the micro- and nano-scales. The surface is different from the bulk and the bulk itself contains many grains, intermetallic phases, inclusions, segregated elements at the grain boundaries, etc [1, 2] (Fig. 1). For these reasons, a variety of microanalytical and microstructual techniques are necessary to characterize, in a volume as small as possible, the elemental composition, the chemical state of the major and minor elements present and their distribution in the three dimensions. Conventional techniques like optical microscopy (OM), scanning electron microscopy (SEM), electron probe microanalysis (EPMA), scanning transmission electron microscopy (TEM/STEM) have been well established for many years. New techniques like the nuclear microprobe (NM) [3],

0022-2461/88 $03.00 + .12 © *1988 Chapman and Hall Ltd.*

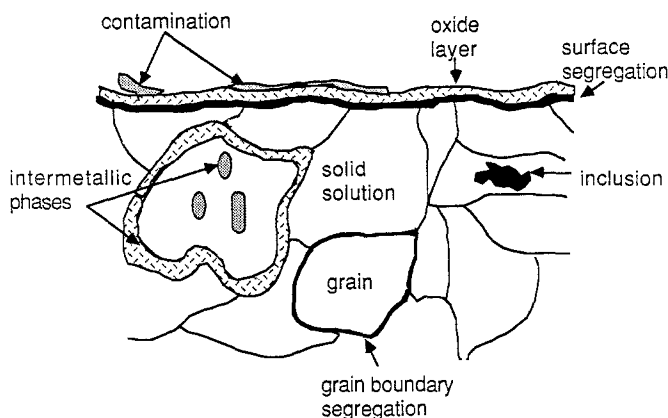

Figure 1 Schematic representation illustrating the heterogeneous nature of typical metallurgical samples, showing a superficial contamination layer, the surface oxide, grains, inclusions, intermetallic phases, segregation at the surface and at grains etc.

focused synchrotron radiation (FSR) [4], the field ion microscope (FIM) and the atom probe (AP) [5] provide very novel information on the "bulk" of metallurgical samples. Superficial information is provided by X-ray photoelectron spectroscopy (XPS or ESCA), scanning Auger microscopy (SAM) [6], scanning tunneling microscopy (STM) [7], ion scattering spectroscopy (ISS) [6] and by secondary ion mass spectrometry (SIMS) [8, 9].

The SIMS technique is not limited to surface analysis of as-received specimens, and due to its broad field of application is increasingly used as a powerful tool for the microcharacterization of solid materials:

(i) every element in the periodic table (from hydrogen to uranium) can be detected at an absolute level of 10^{-15} to 10^{-19} g and at a relative concentration of 10^{-6}(p.p.m. or $\mu g\, g^{-1}$) to 10^{-9}(p.p.b. or $ng\, g^{-1}$);

(ii) SIMS constitutes an "analytical microscope" [8] able to visualize the repartition of major and trace elements in three dimensions, laterally in the (x, y) plane by ion micrographs at a given depth z from the surface (after erosion or using polished cross-sections);

(iii) isotopes can be used as tracers to study chemical reaction mechanisms such as oxidation, corrosion and the hydration of surface layers.

However, the application of SIMS to real complex samples appears to be difficult for reasons specific either to the technique or to the sample itself. These are listed below:

(i) matrix effects revealed in the ion emission: the measured ion intensity is generally not directly proportional to the concentration C of an element [8, 9];

(ii) high complexity of the panoramic mass spectra which include monoatomic and polyatomic ions;

(iii) heterogeneity of the microstructure.

Practically, these problems can be at least partially solved by employing:

(i) standard samples of similar structure and composition;

(ii) a high mass resolution to interpret correctly the complex mass spectra and to select the signal characteristic of the desired species (atomic or molecular);

(iii) an imaging system with a good lateral resolution allowing the selection of a homogeneous small area which can be analysed without any ambiguity;

(iv) other techniques like SEM, EPMA, TEM/STEM and NM, providing invaluable complementary information.

In this paper, we shall first present the principles of the SIMS technique and then illustrate typical examples of the characterization of metallurgical materials by following a logical approach for the investigation of an unknown sample: qualitative elemental analysis by mass spectra at low mass resolution, chemical state information by molecular ions, peak identification at high mass resolution, lateral distribution of species (atomic and molecular) by ion imaging, quantitative bulk analysis in the solid solution and within phases, surface, thin film and interface analysis by depth profiles. The unique interest of using isotopic tracers will be recalled.

2. Principles of SIMS

The theoretical and instrumental aspects of SIMS have been widely described in the literature [9]. Only the essential features related to metallurgical applications are presented in the following. As outlined in Fig. 2, four steps are involved in SIMS characterization:

(i) the *bombardment* of the sample, under high vacuum, by primary energetic particles (normally ions, occasionally neutral atoms) in the keV range;

(ii) the *sputtering* of the most superficial layers; the sputtered material consists largely (> 99%) of secondary neutral species, with a small fraction (< 1%) of secondary ions (positive and negative);

(iii) the *extraction* of the emitted secondary ions prior to their injection into a mass spectrometer which *filters* the different species according to their mass/charge ratio; different types of mass spectrometers can be used: quadrupole, time of flight, magnetic, cyclotron resonance [10];

(iv) the *detection* of the secondary ions with a large dynamic range (10^{10}) in intensity I (c.p.s.).

2.1. Mass spectrometry

The basic information is a mass spectrum which represents the ionic intensity I (c.p.s.) corresponding to each isotope against its mass M (a.m.u. or daltons) (Fig. 2, bottom). The initial identification of the elements is obtained from the nominal mass and from the known isotopic distribution, e.g. in Fig. 2, one

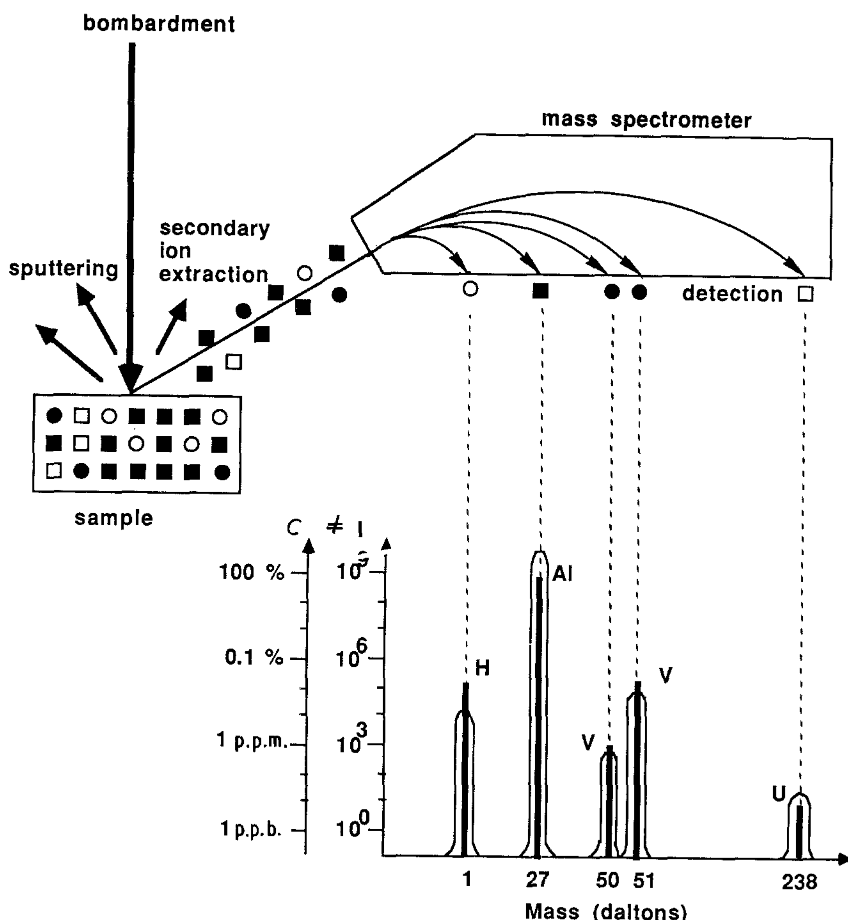

Figure 2 Schematic representation of the principles of SIMS analysis: bombardment by primary projectiles (ions, neutral particles), sputtering of the uppermost layers of the sample, extraction of the secondary ions and filtering by a mass spectrometer (here a magnetic mass spectrometer) and detection of the different filtered species in a large dynamic range (10^{10}). The assumed concentrations C of elements are schematized by dark bars in the mass spectrum $I = I(M)$ which contains the enlarged experimental peaks of intensity I. The symbols in the sample represent atoms of different elements (hydrogen, vanadium and uranium in an aluminium matrix).

isotope (100%) for aluminium at 27 daltons and two isotopes for vanadium at 50 (0.24%) and 51 (99.76%) daltons. If atomic elemental ions (X^+) were the only peaks present in a mass spectrum, as suggested by the oversimplified schematic illustration in Fig. 2, a modest mass resolution would be sufficient to distinguish between adjacent peaks: for instance, one mass unit for the two isotopes 50 and 51 of vanadium. Unfortunately, the mass spectrum of a complex material additionally contains numerous complex ions often considered as "interference" peaks: polymers X_n^+, hydrides XH^+ oxides XO^+, hydroxides XOH^+, intermetallics XY^+, multicharged X^{n+} etc. The probability of finding these complex species increases when the number and the concentration of the elements present in the sputtered volume increase. As a result, to correctly identify monoatomic peaks in a complex spectrum (especially those corresponding to trace elements of low intensity), it is absolutely necessary to be able to resolve, at each nominal mass M, the possible different peaks (m_0, m_1 and m_2, m_n...) (Fig. 3) which are only differentiated by their mass defect ΔM. Up until now, this was only possible with magnetic sector mass spectrometers capable of high mass resolution ($M/\Delta M$ = 3000 to 20000). In the near future, time-of-flight and cyclotron resonance mass spectrometers [10] will also

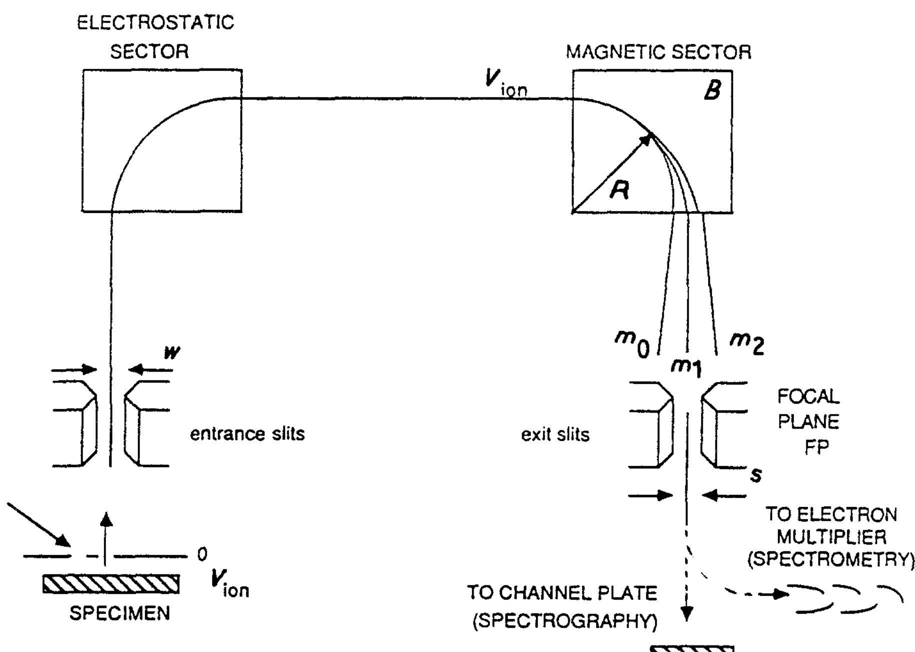

Figure 3 Schematic diagram of a double-focusing mass spectrometer working at high mass resolution. Variable radius of curvature R leads to different positions of resolved peaks m_0, m_1 and m_2 in the focal plane FP of the instrument. Spectra may be acquired in two modes: (i) the mass spectrographic mode (magnetic field B fixed), where the *simultaneous* projection of m_0, m_1 and m_2 on a channel plate allows the display of a narrow portion of the mass spectra as an ion micrograph (ion microscope Cameca IMS 3f); and (ii) the mass spectrometric mode (magnetic field B scanned), where *sequential* detection is performed by a secondary electron multiplier in a fixed position (R fixed).

be operational for high mass resolution SIMS. This essential spectrometric aspect of SIMS characterization will be intensively illustrated in the presented metallurgical applications.

The *unavoidable* presence of molecular species may, however, provide a useful tool as the complex molecular ion spectrum constitutes a "fingerprint" [11] of the sample which can be used for chemical state information or for the identification of intermetallic phases.

2.2. Primary beam

In opposition to the conventional techniques for which the primary excitation is rather rigidly defined (electrons, photons of given energy), the number of degrees of freedom associated with the primary projectile in SIMS is large and the experimental conditions have to be defined with respect to the nature of the problem to be solved. For a primary ion beam, the mass, the chemical nature (inert rare gases, reactive gases (oxygen, nitrogen), metallic ions (gallium, indium, caesium, etc.), the isotopic nature (^{16}O, ^{18}O), the energy (1 to 20 keV) and the incident angle all influence the ion–solid interaction and the probability P for a given species to be emitted as an ion.

The incoming flux of charge brought by a primary ion beam is not exactly compensated by the outgoing flux of charge due to secondary ions or secondary electrons. For conducting samples – the general case for metallurgical materials – the net charge is easily evacuated. However, for poorly conducting materials (ceramics, compounds, polymers etc.), a net charge builds up on the specimen and disturbs the emission and the collection of the secondary ions. Some palliatives are possible. For primary ion bombardment an auxiliary electron gun may be used for charge compensation [12, 13]. Alternatively, charge build-up may be partially avoided by bombarding the sample with a neutral "fast atom beam" (FAB) [14, 15]. This latter can be produced in the primary column by neutralization of the ions in a collision chamber filled with a gas of the same nature. Unfortunately, a FAB source cannot be focused into very small spot sizes.

2.3. Ion–solid interaction

The ion–solid interaction may be controlled over a very wide range, commonly split into two discrete domains; static and dynamic SIMS [9].

The so-called "static" SIMS refers to operating conditions chosen to reduce the primary flux density to very low values of $< 10^{-9}$ A cm^{-2}, or $< 10^{10}$ ions cm^{-2} sec^{-1} [16]. The basic and highly dynamic phenomenon of sputtering remains, but the term static is used as the sample surface remains quasi-unchanged throughout the analysis; the sample surface has to be bombarded for about 10^4 sec to receive an ion dose equivalent to a monolayer. This means that a surface atom hit by a primary ion has a negligible probability of being hit a second time. Provided that ultra-high vacuum conditions are satisfied to avoid surface contamination, static SIMS is particularly well adapted for the study of very superficial phenomena, like the first stages of the oxidation of metals, adsorption on solids [17], etc. Static SIMS is also used for the study of fragile organic materials [18].

The more commonly employed "dynamic" SIMS includes primary flux densities of up to 10^{-3} A cm^{-2} or 10^{16} ions cm^{-2} sec^{-1}, e.g. erosion rates in the low nm sec^{-1} range. The majority of applications given in this paper dedicated to metallurgy correspond to dynamic SIMS.

Another important parameter which controls the ion emission is the oxygen surface coverage θ during sputtering [19]. The steady-state value of θ depends on two fluxes: (a) the flux of oxygen coming from the atmosphere surrounding the sample and (b) the flux of oxygen sputtered away. At low oxygen pressure ($< 10^{-7}$ torr), θ can be considered as close to zero. In this so-called "kinetic" regime, the secondary ion intensity varies linearly with the primary ion intensity I_p. This is illustrated for Al^+ emitted from an aluminium matrix in the lower curve of Fig. 4 [20]. At high oxygen pressure ($\approx 5 \times 10^{-5}$ torr), the Al^+ signal also varies linearly with I_p up to a saturation value ($\approx 1\ \mu$A in the upper curve of Fig. 4) but it is 100 times more intense than in the previous case. This linear regime corresponds to $\theta = 1$ and is known as the "chemical" regime. At intermediate pressure ($\approx 5 \times 10^{-7}$ torr), the Al^+ signal starts by following the chemical regime when I_p is low; then, as θ drops below unity due to increased oxygen sputtering, decreases and finally obeys the kinetic regime law. Practically, quantitative analysis has to be performed in conditions where $\theta = 0$ or, more commonly where $\theta = 1$, this latter is achieved by flooding oxygen at the surface or by bombarding directly with oxygen ions [21]. Secondary ion signals are thus optimized and stabilized. This practice will be abundantly illustrated in the following examples.

Although SIMS is by nature a destructive method, it is possible to control the geometry (x, y, z) of the sputtered volume: typically between 10^{-8} and 10^{-14} cm^3 (Fig. 5). For instance, a volume of 10^{-12} cm^3 may correspond to a very flat volume (a monolayer of 0.3 nm in thickness and 200 μm $\times$ 200 μm area) or to a cubic volume of 1 μm in size. The former case

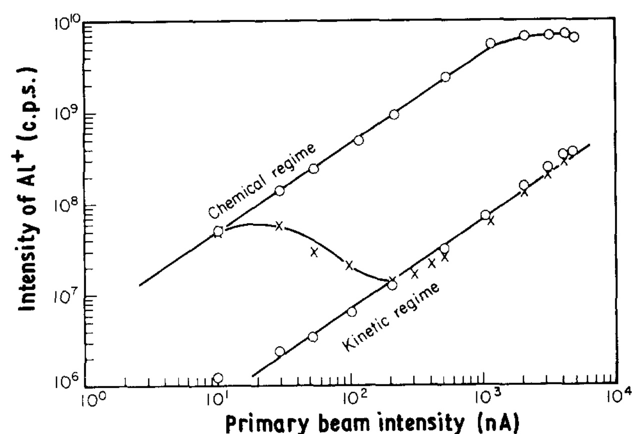

Figure 4 Influence of the oxygen surface coverage θ on the Al^+ signal when an aluminium sample is bombarded by Ar^+ ions (8 keV). (O) Chemical regime ($\theta = 1$), $P_{O_2} = 5 \times 10^{-5}$ torr, and kinetic regime ($\theta = 0$), $P_{O_2} = 1 \times 10^{-7}$ torr; (x) intermediate pressure $P_{O_2} = 5 \times 10^{-7}$ torr.

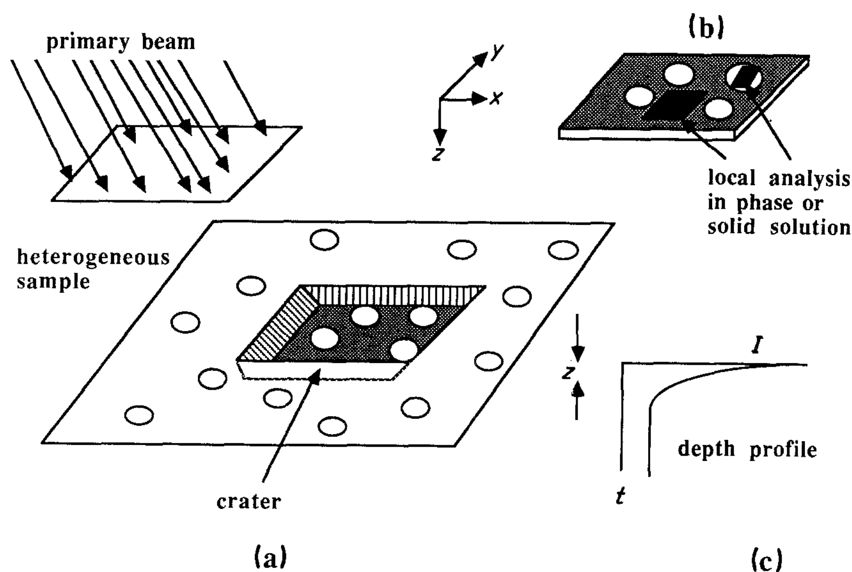

Figure 5 (a) Schematic diagram of the crater of depth z formed after ion sputtering. (b) The lateral (x, y) distribution of elements can be imaged with a finite, but very low thickness z. (c) Selection of a small area of homogeneous composition allows the determination of a significant depth profile $I(t)$.

corresponds to surface analysis and the latter case to local microanalysis. This flexibility provides three analysis modes: at a local point, a one-dimensional profile along a line or two-dimensional for chemical mapping (ion micrographs).

2.4. Lateral distribution of atomic and molecular species by ion micrography

From an instrumental point of view, ion micrographs can be obtained in two ways: simultaneous (direct) imaging with an ion microscope and sequential imaging by a scanning ion microprobe.

In an ion microscope (Fig. 3), every pixel of information is imaged at the same time by stigmatic ion optics [22]. The typical lateral resolution of 1 μm is first defined by the size of contrast diaphragms and ultimately by the optical aberrations of the instrument; it is independent of the size of the primary beam. This is particularly advantagous using a neutral beam (FAB), which cannot be focused, to analyse non-conducting samples [15] (cf. Section 2.2). With the use of ultra-sensitive detectors allowing the visualization of single ions, it is possible to work at lower intensity, for instance:

(i) with reduced diaphragms and hence with an optimized resolution, recent work has shown that a lateral resolution of 0.4 μm [23, 24] could be reached;
(ii) for trace element distribution;
(iii) with molecular ions for chemical state information or identification of intermetallic phases.

Ultra-sensitive detectors coupled with image processors are now able to integrate, average and store digitized images and so provide the final ion micrographs which are immediately available for metallurgical interpretation in real time [23, 25]. Unless mentioned, all micrographs presented in this paper were obtained by a direct-imaging ion microscope (Cameca IMS 3f) [26].

In a scanning ion microprobe [27], the surface is scanned by a finely focused primary ion beam and the resultant secondary ion image is displayed on a synchronously scanned CRT in the same manner as an SEM. The spatial resolution depends directly on the size of the primary beam. The best conventional primary ion columns provide beams of typically 1 μm in diameter. With the development of high brightness liquid metal ion sources (LMIS), probes of 0.02 to 0.10 μm in size are now available and ion micrographs at very high lateral resolution (20 nm) have been recently published [28]. However, to obtain such small ion probe sizes the primary beam current is severely limited, and in practice ion images are essentially limited to major elements, or elements with a high ionization probability. These impressive improvements will certainly play a key role in the future for material characterization by SIMS.

For the same primary density at each pixel, the acquisition time of an image containing N pixels ($\approx 10^4$) is N times lower in an ion microscope than in an ion microprobe [22]. Whatever the imaging mode used, the resulting micrographs in the (x, y) plane always correspond to a finite thickness z. The value of z typically varies between 0.3 nm to several nanometres depending on the volume (xyz) needed to be sputtered to obtain a statistically significant image (Fig. 5b).

2.5. In-depth analysis

In an area of homogeneous composition (Fig. 5b), the variation in the ion intensity I of an element X with the erosion time t reflects the actual depth profile; concentration C with depth z. A quantitative exploitation of the experimental profile $I(t)$ needs a double calibration: I against C (Section 2.6) and t against z. This latter can be performed by measuring with stylus techniques the crater depth obtained after a known erosion time (Fig. 5c). Depending on the primary current density (Section 2.3), the sputtering rate may vary between a fraction of nm sec^{-1} and several nm sec^{-1}. Depending on the primary energy and the incidence angle the depth resolution, defined as the broadening of the signal of A^+ and B^+ at a very sharp A/B interface, lies in the nanometre range [9].

2.6. Quantitative analysis

Finally, when an element has been identified with certainty at high mass resolution, an essential problem

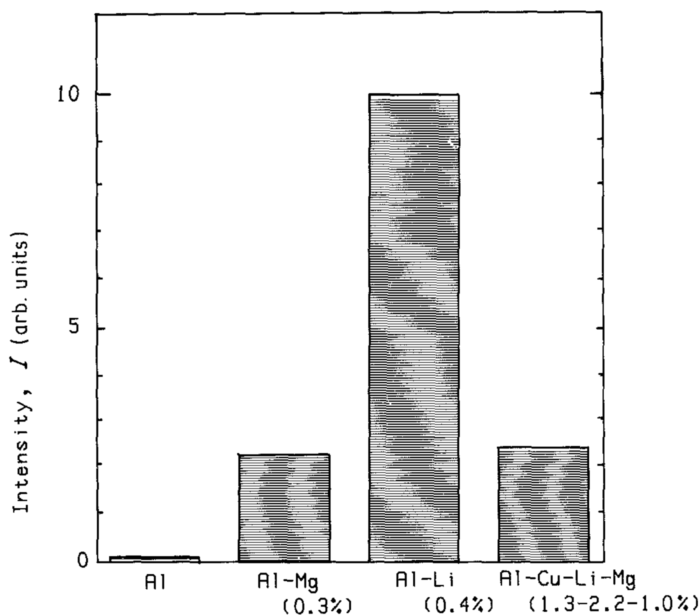

Figure 6 "Matrix effects" in SIMS illustrated by the strong variation of the Al^+ ion signal emitted from a pure aluminium sample and aluminium containing different alloying elements (magnesium, lithium and copper). Ar^+ bombardment at 8 keV.

remains: the conversion of the ion intensity I into concentration C at every point of the sample. Unfortunately, I does not reflect simply C (as outlined by bars in Fig. 2); I depends also on the sputtering yield S (atoms ion^{-1}) and on the ionization probability P according to [8, 9]

$$I \propto SPC \qquad (1)$$

Variations of S could be measured for different matrices. For P, it is very difficult and no theoretical model can help the analyst at the present time. P can vary by several orders of magnitude depending on the chemical composition, e.g. on the electronic state of the sample surface during sputtering, as seen in Fig. 4 concerning the effect of O_2 flooding. For instance, strong variations of ion intensity, so-called "matrix effects", are observed in the following cases:

(i) for the same element X present at the same concentration in different matrices;

(ii) for different elements present at the same concentration in a given matrix;

(iii) for different matrices;

(iv) for the matrix element when a second or a third element is added at relatively low concentration.

This latter is illustrated in Fig. 6 by the strong variation of the ion intensity of the Al^+ ion emitted from a pure aluminium sample and aluminium alloys containing different alloying elements (lithium,

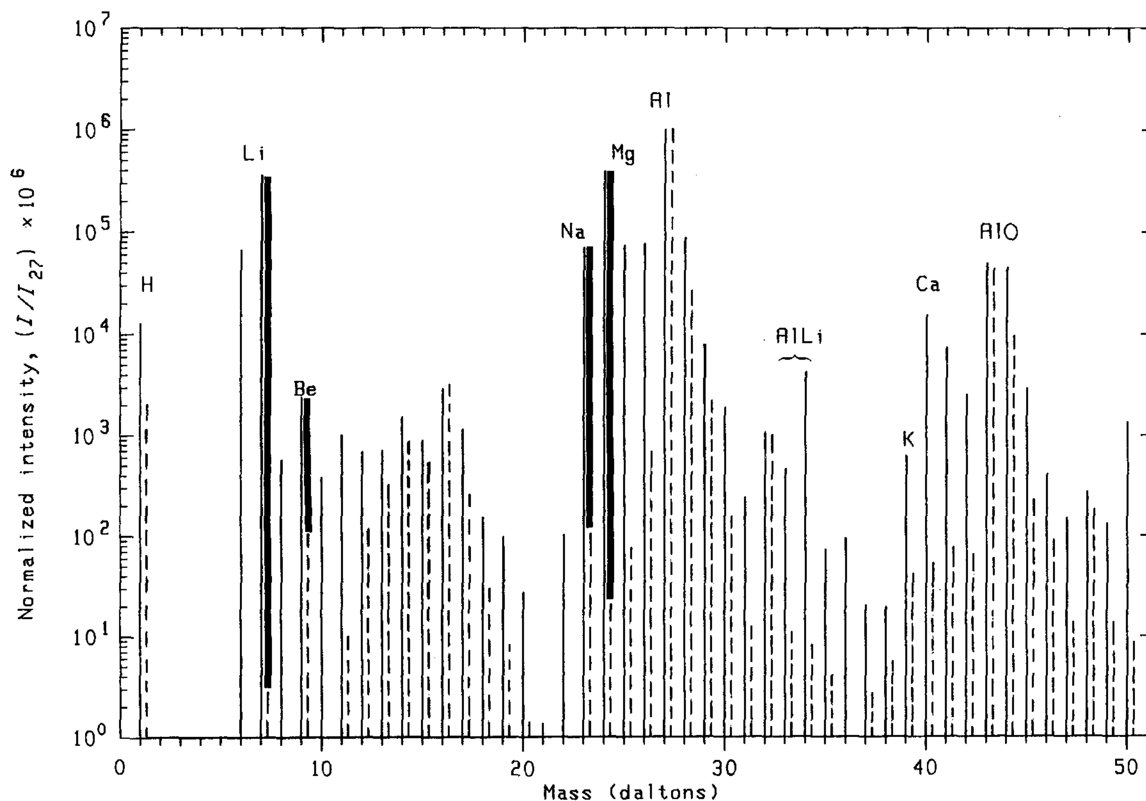

Figure 7 Comparative bar-graph mass spectra of positive secondary ions corresponding to a (——) superficial oxide layer (4 nm thick) and (– – –) the bulk aluminium substrate. Intensities are normalized to the matrix ion $^{27}Al^+$. Low mass resolution ($M/\Delta M$ = 300). Dark bars at 7, 9, 23 and 24 daltons represent the concentration *ratio* of lithium, beryllium, sodium and magnesium between the surface and the bulk [32]. Ar^+ (2.5 keV) + O_2.

magnesium, copper between 0.3 and 2.2 wt %), all other operating conditions being maintained rigorously constant. The matrix effects are not easy to overcome in metallurgical samples since the composition is susceptible to change abruptly from point to point. New ways are being investigated to attenuate or to suppress these matrix effects, for instance by post-ionizing the sputtered neutral species (independent of *P*) and by rejecting the true secondary ions. Post-ionization can be performed in several ways: electron impact [29], plasma [30] and laser [31].

3. Qualitative analysis of metallurgical samples by mass spectra

3.1. Panoramic analysis at low mass resolution

A rapid mass spectrum at low resolution ($M/\Delta M \leqslant 300$) of the positive and negative secondary ions gives a rapid survey analysis down to the p.p.m. level. According to Equation 1, as the ionization probability *P* for the different elements in a given matrix is, *a priori*, not known, the ion intensities are not a simple reflection of the concentrations of the relative components. Such spectra are interesting in the *comparative mode*, i.e. between different locations (laterally or in depth) on the same sample or between different samples of similar composition. Fig. 7 represents the spectrum between 1 and 50 daltons of:

(i) the typical 4 nm thick oxide layer which covers any aluminium sample, and
(ii) the bulk (i.e. $\approx 1\,\mu$m deeper).

As the sputtered matrices are very similar in nature (natural oxide and oxide dynamically created by oxygen flooding on the sample surface) [20], the basic (fingerprint) spectra constituted by the complex molecular ions are also similar: see for instance AlO^+ at 43 daltons. In this comparative mode, at each nominal mass, the contributions of complex ions from the matrix material cancel out and the difference in intensity reflects a difference in the possible remaining ions. For atomic ions this represents, to a first approximation, the difference in concentration of impurities present at the two sample depths. For instance, at masses 7, 9, 23 and 24 daltons, thick bars in Fig. 7 suggest that lithium, beryllium, sodium and magnesium are more concentrated at the surface than within the bulk. A more detailed and quantitative description of the surface enrichment of these elements [32] will be given in the depth profiles of Fig. 27 in Section 6.1.1.

Practically, mass spectra are directly recorded in computer memory and stored on tape or disc. Software routines allow rapid data treatment, providing a means of extracting the maximum benefit from mass spectra which are inherently rich in information but extremely complex. For example, to compare two similar materials it is possible to obtain several mass spectra from each and perform a statistical evaluation at each nominal mass to determine if there is a significant difference or not. Similarly, to determine the secondary ions characteristic of an interface region between two matrices (Section 6.2.3), it is possible to use peak normalization and subtraction routines.

3.2. Chemical state information by molecular ions

For the elemental analysis in the preceeding section, it was necessary to suppress the influence of molecular ions in mass spectra. Conversely, the complex ions can be used to provide chemical information. In Fig. 7, the metallic oxide ion $^{27}Al^{16}O^+$ at 43 daltons suggests that aluminium and oxygen atoms were next-neighbours in the sample before sputtering. In the same way, the existence of intermetallic ions $^{27}Al^{6}Li^+$ and $^{27}Al^{7}Li^+$ at 33 and 34 daltons means that aluminium and lithium atoms were next-neighbours in the solid solution or in intermetallic phases. This behaviour is quite general. For instance Namdar [33] could, in the Fe–O system, distinguish between the three iron oxides Fe_2O_3, Fe_3O_4 and FeO in the sample by monitoring the significant change in the intensity of the Fe_3O^+ ion.

By using pattern recognition techniques, Wilhartitz and Grasserbauer [34] were able to classify different compounds of the same element, e.g. of manganese borides of different stoichiometry. In Fig. 8, the relative intensities of the ions Mn_x^-, B_y^-, $Mn_xB_y^-$ are used in a three-dimensional representation to distinguish the different borides. The differences between the mass spectra of the various borides are much larger than the statistical error of measurement.

3.3. Accurate analysis at high mass resolution

Rigorously, a spectrum obtained at low resolution only allows the presence of elemental or molecular ions to be presumed. The certitude comes only after having

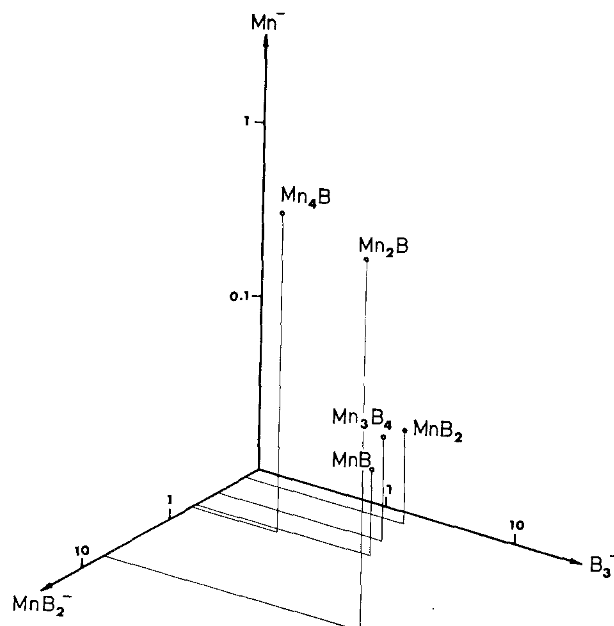

Figure 8 Computer-based microanalysis: direct phase identification by evaluation of the fragmentation of secondary ion mass spectra with pattern recognition techniques. Mass spectra of MnB and MnB_2 and representation of molecular and cluster spectra of manganese borides by classification pattern, showing the potential to identify different compounds. Circles around the points represent the statistical error of measurement of the mass spectra (trivariate plot) [34].

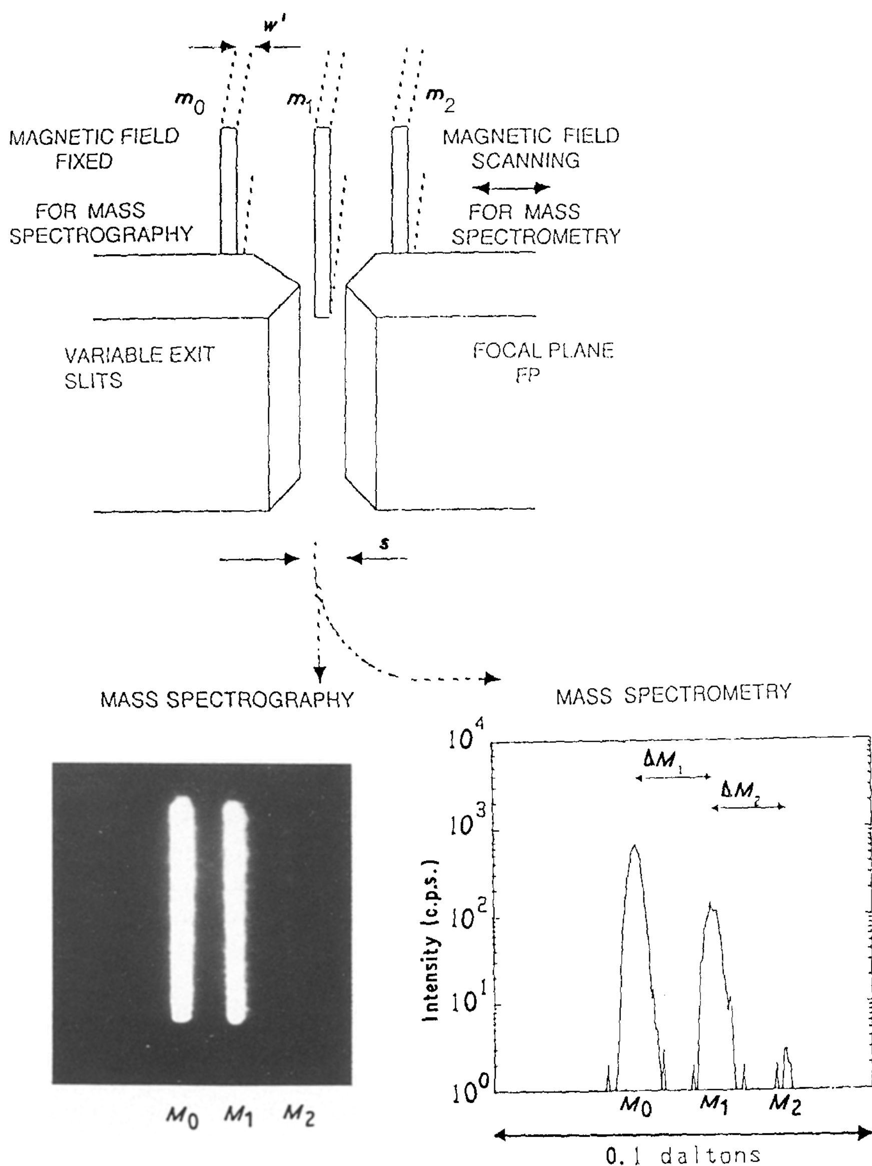

Figure 9 High mass resolution spectra at 56 daltons of an aluminium alloy matrix–SiC fibre composite material. In the mass spectrometric mode at a resolution of 8000 (bottom right) both polyatomic combinations of major elements and iron impurity are clearly observed. The same spectrum in the direct imaging mode (mass spectrographic), but at a resolution of 16 000, is presented at the bottom left. Peaks M_0, M_1 and M_2 are identified as $^{56}Fe^+$, $^{28}Si_2^+$ and $^{24}Mg_2\,^{16}O^+$, respectively [35].

resolved and identified the peaks present in a multiplet (m_0, m_1, m_2 in Fig. 3) at a nominal mass by using a mass spectrometer characterized by a high mass resolving power ($M/\Delta M$ = 2000 to 20 000 as defined at 10% peak height).

Until now, magnetic mass spectrometers were essentially used for this purpose. In the mass spectrometric mode, the magnetic field is varied within a narrow mass range ($\approx \pm 0.1$ daltons) so as to scan the image of the entrance slit across a fixed exit slit. This is illustrated [35] in the bottom right corner of Fig. 9 at 56 daltons where iron is expected to be present in an SiC fibre-reinforced aluminium alloy matrix composite material. Three peaks are clearly resolved: Fe^+, Si_2^+ and MgO_2^+; they come respectively from a matrix impurity, from the ceramic fibres and from the alloy itself.

In instruments specially designed to provide direct imaging like the Cameca IMS 3f (Fig. 3) [23,26] ion microscope, the resolved spectrum in the exit focal plane can also be directly displayed (spectrographic mode, cf. also Section 4), even for very low intensities. Such a spectrum is shown in the bottom left of Fig. 9. Compared to the dynamic spectrometric mode, the static spectrographic mode allows the simultaneous detection of every peak without possible loss of information, for instance when their relative intensities are susceptible to rapid change (heterogeneity in depth). In addition, the mass resolution is roughly twice that in the spectrometric mode, or, put another way, for the same mass resolution the count rate is double.

Until recently, the identification of the resolved peaks, i.e. the determination of their exact mass and the attribution of a chemical formula, was a tedious procedure involving trial and error sequences with supposed known masses. To eliminate any ambiguity and to improve the response time, we have successfully developed a new procedure [35], involving the sequential analysis of the unknown sample and of a reference sample providing well identified peaks (matrix etc.). The direct superposition of the two spectra, obtained in either the spectrometric or spectrographic mode, allows a simple calculation of the exact mass of all unknown peaks. The relative precision in the mass determination lies in the 10^{-5} range. For instance the experimental mass of M_1 in Fig. 9 was found to be 55.9555 for a theoretical value of 55.9539 corresponding to $^{28}Si_2^+$. The full benefit of this technique is found in the spectrographic mode, but requires ultra-sensitive image detection and on-line image storage/analysis to achieve its optimum performance.

Due to the presence of interference (molecular)

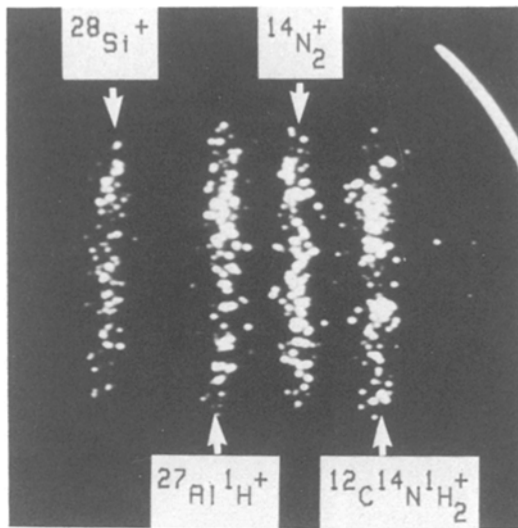

Figure 10 Mass spectrography spectrum obtained at 28 daltons on carbon fibres. Due to the bombardment conditions the total count rate for the four peaks was about 20 c.p.s., requiring integration for 63 sec. The mass resolution $M/\Delta M$ is 9000. Ar^+ bombardment at 8 keV [35].

peaks (Section 4.2) which often submerge the species under investigation, the necessity of having well-resolved *and* identified peaks is a prerequisite in most applications. For instance, (a) for the quantitative analysis of trace elements ($< 1\,\mu g\,g^{-1}$) in complex materials and (b) for the very superficial analysis of segregated or contamination impurities. In the latter case, the intensity of the peaks of interest change rapidly with time (depth). Fig. 10 illustrates the identification of N_2^+ and Si^+ at 28 daltons in the presence of molecular peaks AlH^+ and CNH_2^+ at the surface of carbon fibres used for the reinforcement of metallic matrices [35]. The inversion of the intensity of the two peaks detected at 64 daltons reveals in Fig. 11 the existence of two phenomena in the thin oxide layer covering an individual grain of Al–Zn powder: an enrichment in magnesium by the molecular ion Mg_2O^+

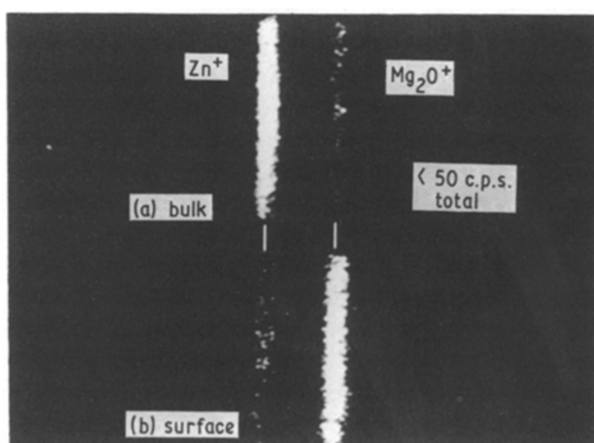

Figure 11 Mass spectrography allows the detection of *transient* peaks, as illustrated by the spectra for an Al–Zn powder at 64 daltons showing two peaks, ^{64}Zn (63.9291) and $^{24}Mg_2\,^{16}O^+$ (63.9650): (a) spectrum from the "bulk" of an individual grain (> 50 nm beneath the oxide) showing the presence of zinc and magnesium; (b) spectrum from the extreme surface oxide region showing a drastic change in the relative intensities of the two peaks. Ar^+ bombardment at 8 keV, mass resolution $M/\Delta M = 13000$ [35].

and a depletion in zinc, one of the constituent elements of the alloy [35].

In summary, experience shows that high mass resolution is a prerequisite if further investigation (cf. Sections 4 to 6) of complex materials science samples is to be undertaken. This does not mean that each analysis will systematically be performed at high mass resolution, but that prior verification allows low-resolution work to be performed with complete confidence.

4. Qualitative microscopy by ion imaging

4.1. Elemental ion microscopy

From a metallurgical point of view, the lateral distribution of constituent elements and of impurities is of prime importance. Indeed, for the same global chemical composition a different partition of major elements between the matrix (solid solution) and the phases will lead to different macroscopic properties. Due to the very low thickness (in the nanometre range) needed for providing significant information, ion micrographs of a heterogeneous structure may be considered as a two-dimensional image or elemental map (Fig. 5b). However, it provides only a qualitative contrast between the different areas of homogeneous composition. Once again the comparative use of ion micrographs is very useful and generally provides a novel insight into the sample under investigation. This is achieved by the superposition of the ion micrographs of the combined elements in a given area.

Complementary information can be obtained by micrographs taken at the same magnification on the same area by other techniques: OM for pre-location and SEM for a semi-quantitative chemical analysis (X-ray emission for atomic number $Z > 5$ and back-scattered electrons for mean Z contrast). For $Z < 5$, only SIMS is able to provide the information. This complementary metallographic approach on the same area is illustrated in Fig. 12 for the case of a new Al–Li aircraft alloy (as-cast alloy) [36]. The optical micrograph (Fig. 12a) exhibits very poor contrast while the SEM micrograph using back-scattered electrons (Fig. 12b) reveals a significant contrast in the interdendritic regions. These black areas are supposed to contain an element lighter than the aluminium matrix, probably lithium. The proof is only given by the ion micrographs (Fig. 12e) which, in addition, bring the following novel information:

(i) the identification of a new ternary phase at the interdendritic regions with superposable micrographs of the monoatomic ions corresponding to aluminium, lithium and magnesium (Figs 12d, e and f);

(ii) direct confirmation of the existence of this phase by the intermetallic ions AlLi and MgLi (Figs 12g and h) (Section 4.2);

(iii) the direct visualization of the solid solution of lithium and magnesium (Figs 12e and f);

(iv) the presence of trace elements in the bulk at the p.p.m. level like hydrogen (Fig. 12c) and sodium (Fig. 12i). Note that the analysis of sodium had to be performed at high mass resolution ($M/\Delta M = 2000$)

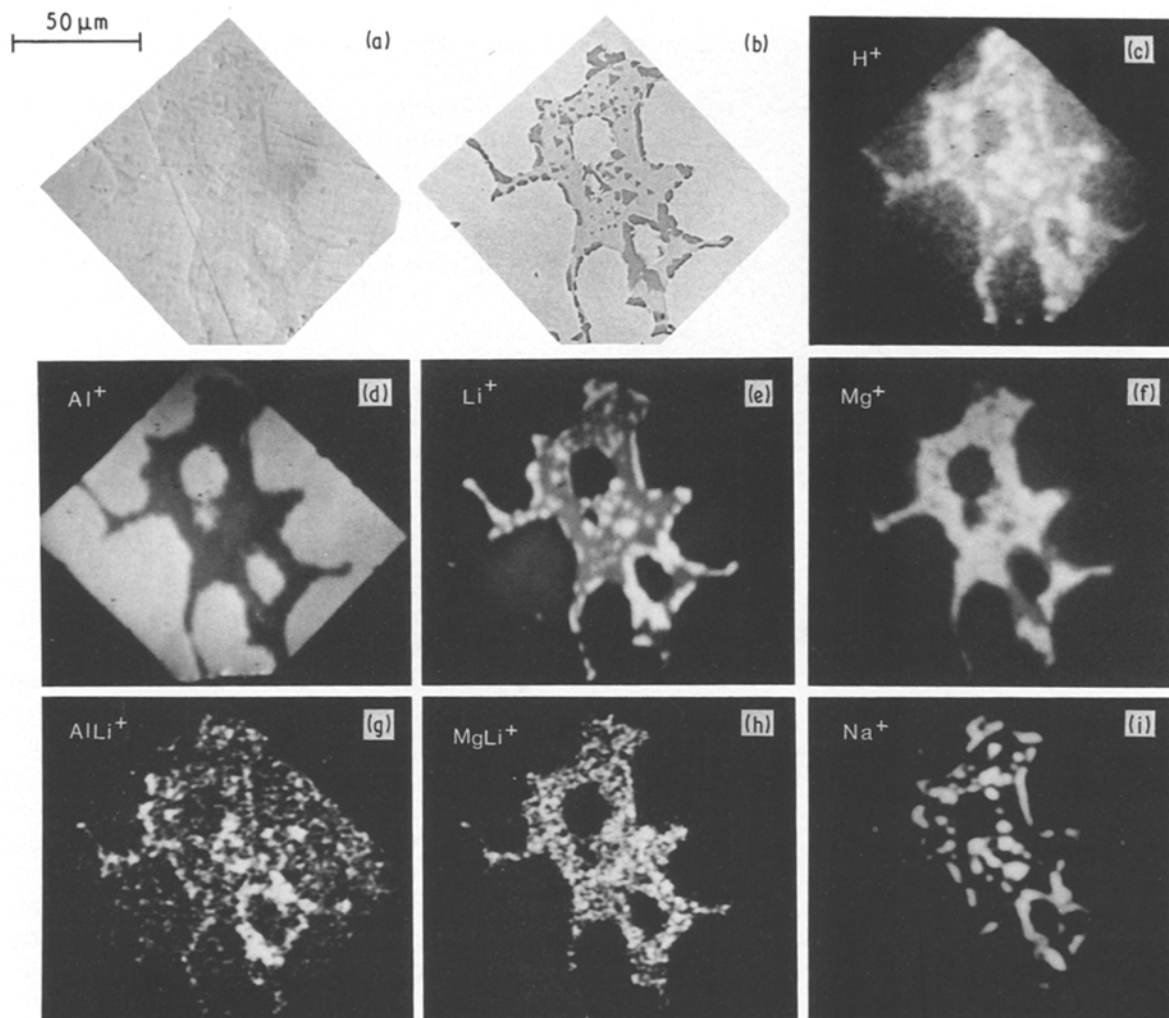

Figure 12 Micrographs obtained at the same magnification on the same area of an Al–Li alloy by (a) optical microscopy, (b) scanning electron microscopy (back-scattered electron mode) and (c to i) SIMS: (d, e, f) the major constituents aluminium, lithium and magnesium; (g, h) the intermetallic ions $AlLi^+$, $MgLi^+$ characteristic of a new intermetallic phase; and trace elements (c) hydrogen and (i) sodium. Cs^+ bombardment at 5.5 keV.

to distinguish the monoisotopic ion $^{23}Na^+$ (22.9898 daltons) and the intense polyatomic matrix ion $^{7}Li^{16}O^+$ (23.0109 daltons).

The unique capability of SIMS to visualize a possible heterogeneous distribution of hydrogen in metallurgical samples has already been exploited [37–39], for instance to demonstrate the embrittlement of niobium by hydrogen.

A specific property of sputtering by inert gas ions can be used in a unique way in metallurgy. A *crystallographic contrast* [40] is observed in the matrix ion micrograph due to the differential sputtering of adjacent grains having different orientation (several degrees). Visually, this structural information can be directly related to chemical information given by the micrograph of any major or minor element. As an example Fig. 13 shows how trace amounts of beryllium (present in the bulk at $0.08\,\mu g\,g^{-1}$, cf. Fig. 27) are able to migrate during heat treatment via grain boundary diffusion to the oxide–metal interface of an aluminium sample [32]. Under the same conditions, other impurities like lithium and magnesium are randomly concentrated in the superficial region, but by a different diffusion mechanism than for beryllium.

Fig. 14 shows ion micrographs at extremely high spatial resolution obtained by Levi-Setti *et al.* [28] with a scanning ion microprobe equipped with a liquid gallium ion source. The sample investigated was an amorphous metal–metalloid alloy (metallic glass) $Fe_{75}B_{15}S_{10}$ crystallized at 900 K for 4 h. The surface of the ribbon exhibits a network of fine shallow crevices. These seem to represent grain boundaries where iron and beryllium segregate, with identical distributions (Figs 14c and d), presumably in an Fe_2B eutectic crystallization phase which appears oxidized at the surface. Similarly, the O^- and Si^+ maps suggest an SiO_2 layer covering most of the sample surface. It is quite evident that high-resolution SIMS imaging will add a new dimension to this area of investigation, by providing an insight which seems needed for a more detailed interpretation of the results obtained by other approaches such as Mössbauer spectroscopy.

4.2. Intermetallic and molecular ion microscopy

The chemical information inherent in the relative intensities of molecular ion species in mass spectra can be taken a step further using ion microscopy. The direct imaging of intermetallic ions such as $AlLi^+$ and $MgLi^+$ (Figs 12g and h), emitted from the same area

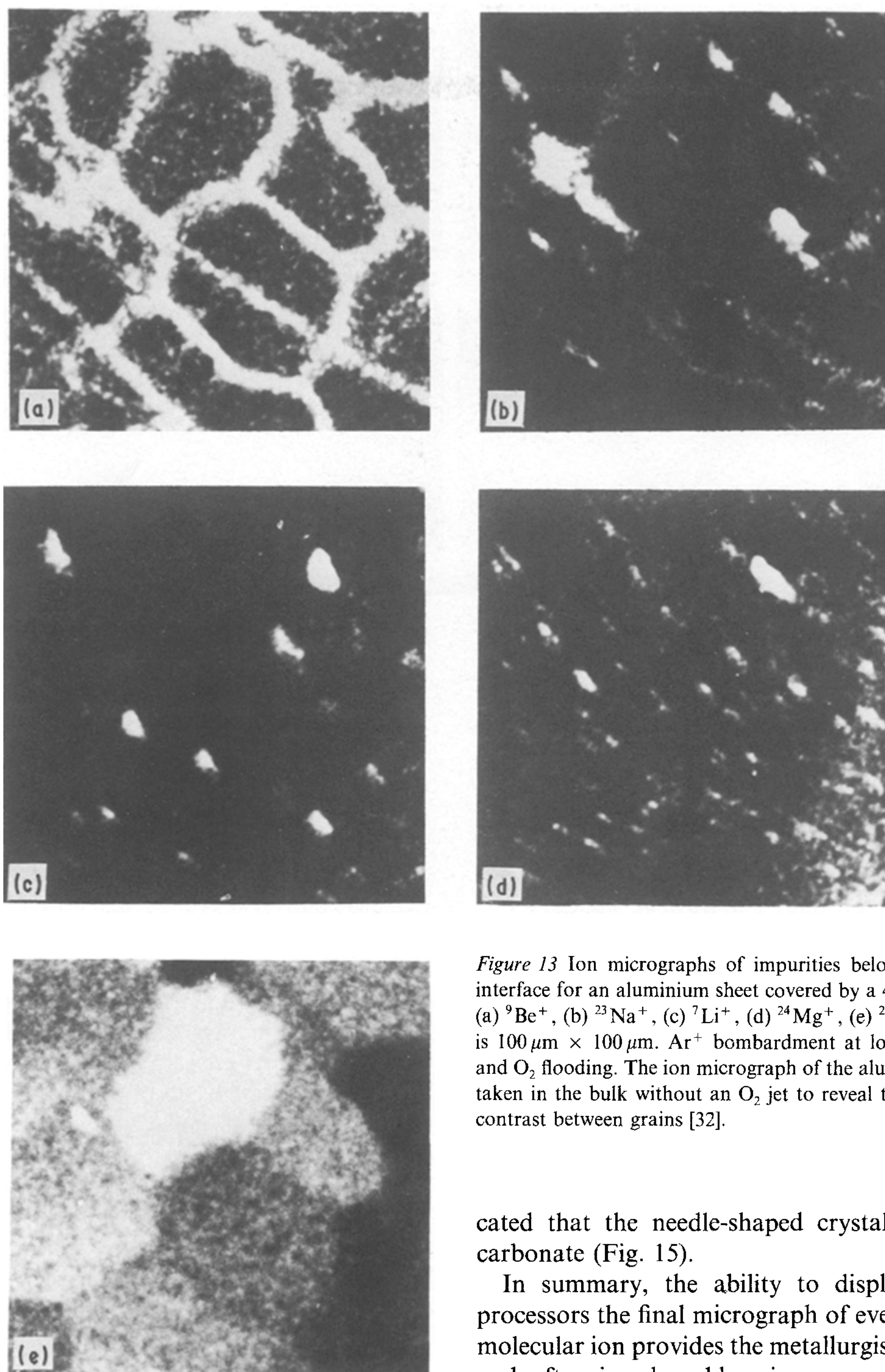

Figure 13 Ion micrographs of impurities below the oxide–metal interface for an aluminium sheet covered by a 4.2 ± 0.5 nm layer. (a) $^{9}Be^{+}$, (b) $^{23}Na^{+}$, (c) $^{7}Li^{+}$, (d) $^{24}Mg^{+}$, (e) $^{27}Al^{+}$. Imaged zone is $100\,\mu m \times 100\,\mu m$. Ar^{+} bombardment at low energy (2.5 keV) and O_2 flooding. The ion micrograph of the aluminium matrix was taken in the bulk without an O_2 jet to reveal the crystallographic contrast between grains [32].

at lower intensity than the monoatomic ions, provides direct evidence of intermetallic phases containing simultaneously these elements. It should be noted that it is often necessary to combine ion microscopy and high mass resolution to resolve certain relatively weak molecular peaks (cf. Figs 9, 10 and 11) [23]. Real-time visualization and interpretation may be assumed by digital image processing routines such as integration and averaging.

A second example concerns the combination of ESCA and SIMS analysis of the surface of an Al–Li alloy exhibiting a thick insulating surface layer containing needle-like crystals. ESCA indicated, among other things, the presence of lithium carbonate on the sample surface, but provided no lateral resolution. FAB SIMS using molecular imaging of $^{7}Li^{12}C^{16}O_3^{-}$ (with a lateral resolution of about 1 μm) clearly indicated that the needle-shaped crystals were lithium carbonate (Fig. 15).

In summary, the ability to display with image processors the final micrograph of every elemental or molecular ion provides the metallurgist with a routine and often irreplaceable microscope for the characterization of heterogeneous metallurgical samples. Qualitative ion imaging also provides the ability to select, by a variable field diaphragm (of down to several micrometres, cf. Fig. 5b) or electronic gate for microprobe instruments, areas of homogeneous composition (matrix or phases) for further characterization (cf. Section 5).

5. Quantitative analysis in the bulk of metallurgical samples

An element present as a constituent or impurity in a given material is distributed within the solid solution or within phases, depending on whether its concentration is lower or higher than the solubility limit. Depending on this distribution, the ion emission is expected to be different according to Equation 1. By matrix, we mean in SIMS an imaged region which appears to be homogeneous on a scale corresponding

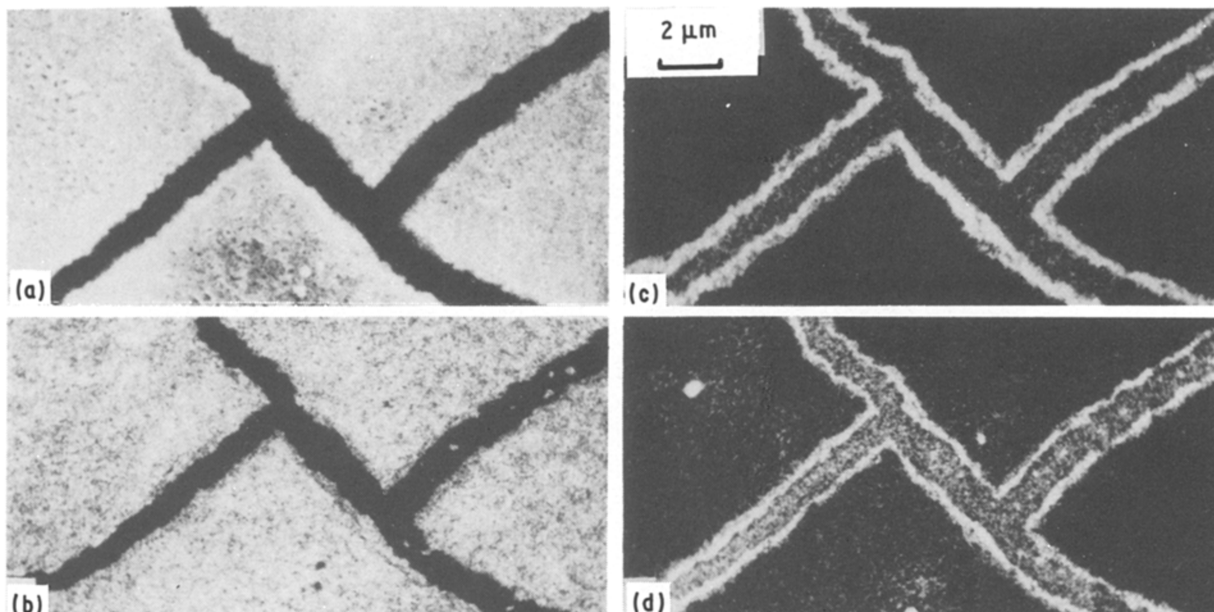

Figure 14 High spatial resolution (20 nm) of major elements in a crystallized amorphous metallic glass. Conditions: 20 pA Ga^+ probe, 512 sec exposures. (a) $^{16}O^-$; (b) $^{28}Si^+$; (c) $^{11}B\,^{16}O_2^+$; (d) $^{56}Fe^+$ [28].

to the resolving power of the instrument (typically 1 μm for ion microscopes). Physically, this may correspond to a true solid solution or to a solid solution including very fine precipitates (in the nanometre range) which are only observable in the TEM.

The importance of the solubility limit is illustrated in Fig. 16 [41] for silicon present in standard aluminium samples at a global concentration ranging between 3 and 3200 $\mu g\,g^{-1}$ (determined by wet chemistry). The normalized intensity does vary linearly with the announced concentration, but within two discrete ranges. Below 700 $\mu g\,g^{-1}$, ion micrographs appear to be homogeneous corresponding to silicon in the matrix; the calibration line passes through the origin. At 700 $\mu g\,g^{-1}$, the phase diagram predicts [42] that a new phase Al–Si–Mn will appear. This is actually confirmed by the ion micrographs of Si^+ (and Mn^+). The area fraction of this silicon-rich phase now defines the ion emission and the slope changes since values of P and S (Equation 1) are different from those of the matrix. A correct analysis of either the matrix or phases requires pre-selection of small areas by using a diaphragm (Figs 5b and 17b) and the calibration with standard samples of similar structure and composition.

5.1. In the matrix

For dilute solutions ($C < 1\%$), matrix effects in SIMS may generally be neglected and calibration lines like those shown in the left part of Fig. 16 are normally obtained provided that standard samples are

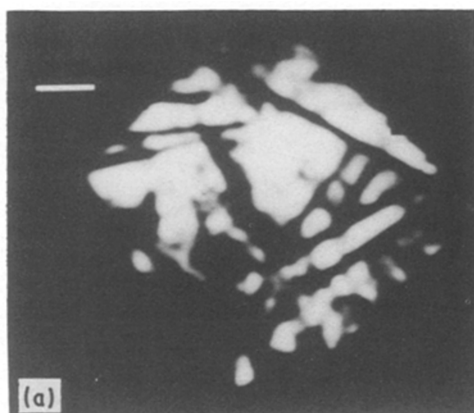

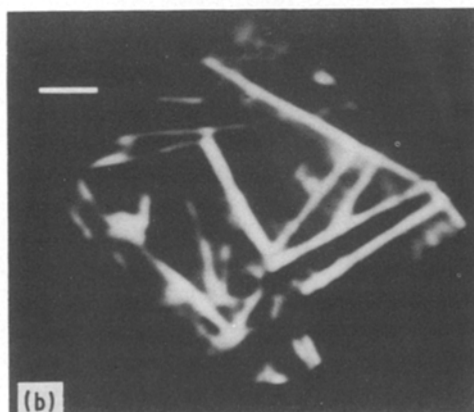

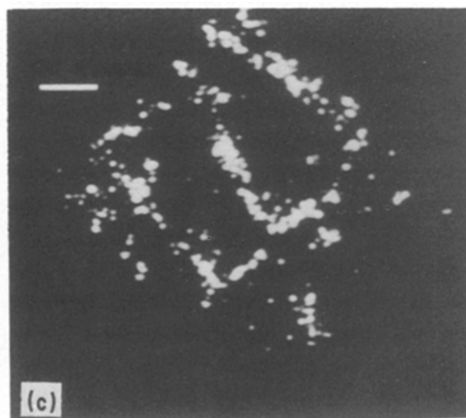

Figure 15 SIMS as a chemical microscope. In the imaging mode, the molecular ion $LiCO_3^-$ forms localized needle-like crystals of lithium carbonate on the complex surface of an Al–Li alloy. (a) $^{27}Al^+$, (b) $^7Li^+$, (c) $^7Li\,^{12}C\,^{16}O_3^-$. The bars represent 20 μm.

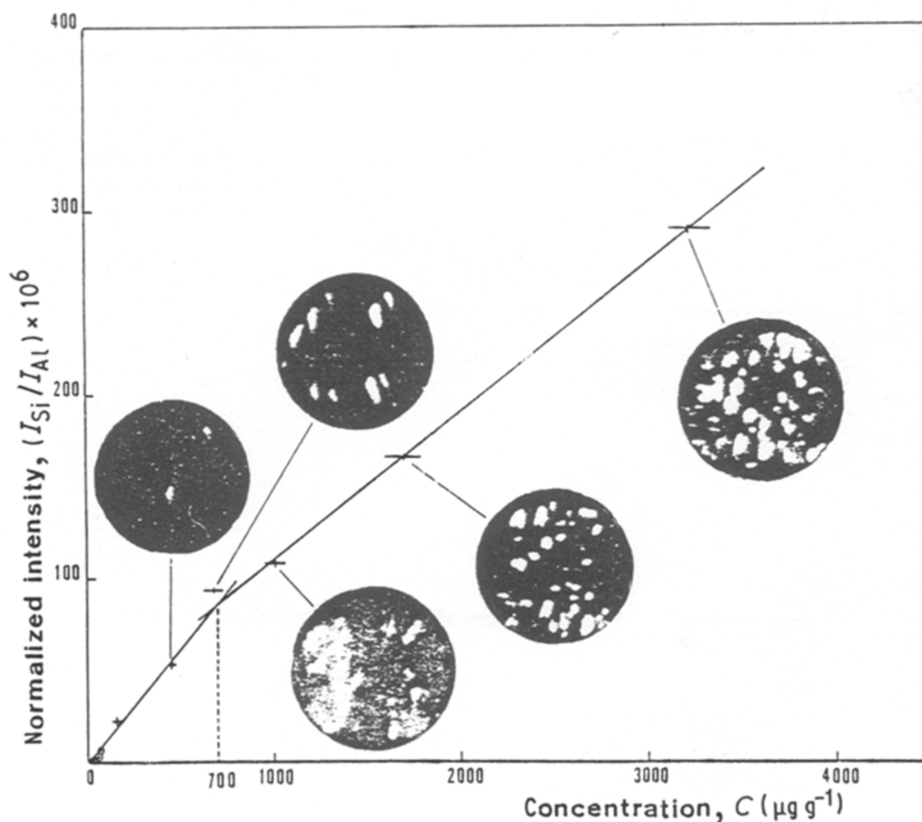

Figure 16 Linear variations of the normalized intensity of $^{28}Si^+$ against the global concentration between 3 and 3200 $\mu g\,g^{-1}$. The change of gradient at 700 $\mu m\,g^{-1}$ corresponds to the precipitation of an Al–Si–Mn phase (cf. micrographs). Below this value, silicon is in solid solution. O_2^+ bombardment at 8 keV and mass resolution $M/\Delta M$ = 3500 [41]. Image diameter = 60 μm, sputtered depth = 14 nm, i.e. 10^{-10} g of material analysed at each data point.

available. In metallurgy, quantitative analyses on a micrometre scale are routinely performed by EPMA [43]. This technique is able to provide standard samples, but with the three following limitations:

(i) inoperative for light elements ($Z < 5$);
(ii) rather poor detection limit (10 to 1000 $\mu g\,g^{-1}$);
(iii) an information depth of about 1 μm which is problematic for fine microstructures since small phases below the surface can contribute to the measured signal and distort the desired analysis of the matrix (hatched area in Fig. 17a).

Provided that the concentration $C > 1\%$, EPMA may be replaced for (i) above (light elements) by a new reference technique, the nuclear microprobe [3]. For (ii) and (iii), SIMS alone can satisfy these requirements. For instance, with its low information depth (in the nanometre range, Fig. 17b), SIMS is virtually two-dimensional and analyses what "is seen'. A homogeneous area between phases can be selected in the ion micrograph of X.

5.1.1. Elements at high concentration within the matrix

Under certain sampling conditions an ion micrograph may be considered as quantitatively representing the two-dimensional distribution of an element and thus quantitative image analysis may be considered. To eliminate spurious effects such as non-uniform response of the detection system, the image of interest is first normalized with respect to the image of the matrix element using an image analyser [23, 44]. Fig. 18a illustrates a normalized $^{24}Mg^+/^{27}Al^+$ image calibrated in magnesium concentration in the as-cast structure of an Al–Li–Mg–Cu alloy (cf. Fig. 12) [23]. Each pixel grey level is now proportional to the concentration and the normalized image may be used to obtain rapidly and accurately the lateral distribution of the element in any chosen direction (along any line), or to obtain a concentration histogram in any selected zone. To illustrate the validity of the approach, Fig. 18b represents the comparison of three techniques used to obtain the magnesium concentration curve along a line in Fig. 18a. Curve 1 is from EPMA, Curve 2 from a conventional SIMS lateral scan obtained by displacing the specimen laterally with respect to the defined analysis zone, and Curve 3 from a lateral pixel analysis of the normalized Mg^+/Al^+ image.

The three scans are not significantly different within experimental error. When interpreting such results, it must be remembered that grain-boundary magnesium-containing intermetallic phases were incorporated in line scans and ion images; within these regions the concentration scale for Curves 2 and 3 are no longer valid due to matrix effects in SIMS (Section 2.6).

As light elements ($Z < 5$) are undetectable by EPMA, the nuclear microprobe [3] can provide a reference method for SIMS. Fig. 19 shows two line-scan analyses of lithium across the outer 250 μm of a polished cross-section of a heat-treated Al–Li (2.8% Li) alloy sheet (800 μm thick). They were performed (i) by SIMS with a lateral resolution of 1.5 μm and (ii) by NM using a 5 μm proton beam (1.2 MeV); detection was performed by the $^7Li(p, \alpha)^4He$ reaction [45, 46]. The normalized profiles given by the two techniques may be considered as superimposable and showed a significant depletion of lithium extending to about 150 μm from the surface at each side of the sheet. Hence, SIMS may be considered as free from matrix effects in this lithium concentration range.

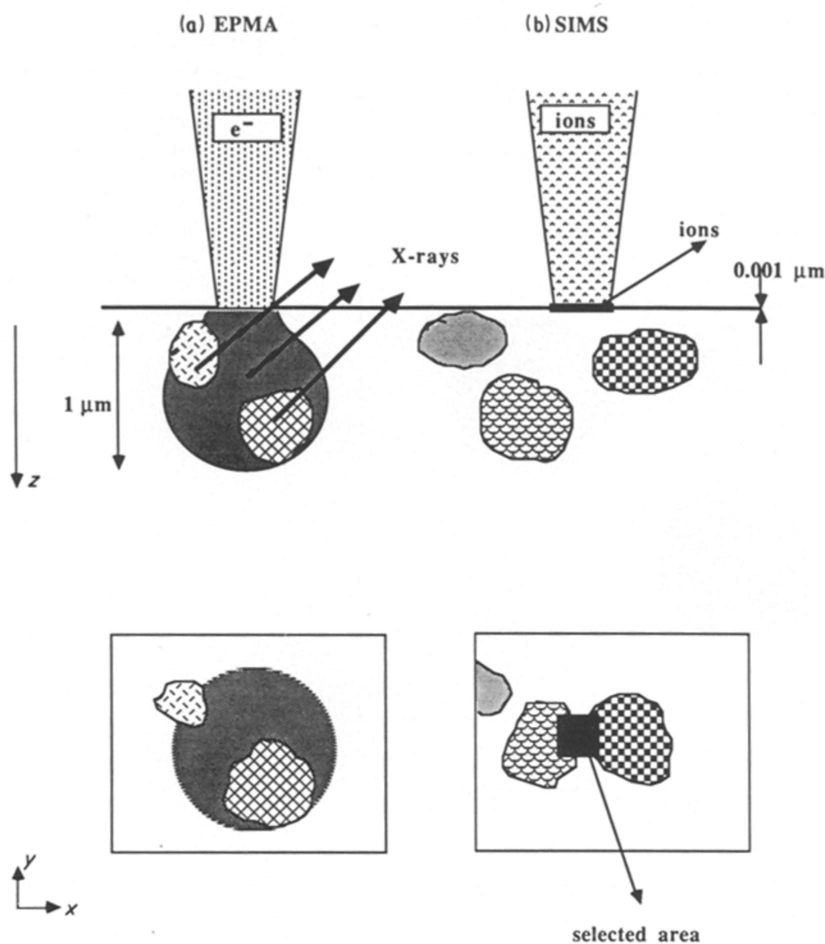

Figure 17 Schematic representation of the information depths in (a) EPMA ($\approx 1\,\mu m$) and (b) SIMS ($\approx 0.001\,\mu m$). For very fine microstructures, a true matrix analysis (hatched areas) is impossible in EPMA since subsurface phases contribute to the signal. In SIMS, an area of homogeneous matrix can be selected for analysis from the ion micrograph.

5.1.2. Elements at low concentration within the matrix

For samples with a very fine structure, an element X may be distributed at high concentration within small phases and at low concentration in the matrix.

How SIMS can obviate the difficulties associated with small phases below the surface during EPMA analysis (Fig. 17a) is illustrated in Fig. 20 for the determination of the solubility limit of iron present at a total, but low, concentration of $105 \pm 8\,\mu g\,g^{-1}$ in a 7X75 aluminium alloy (Al–Zn–Mg–Cu). For different precipitation states corresponding to different heat treatments 1 and 2 (with $T_2 > T_1$), EPMA results obtained at random gave histograms of local concentration ranging between 30 and $300\,\mu g\,g^{-1}$ (Fig. 20a) and between 80 and $170\,\mu g\,g^{-1}$ (Fig. 20b). In both cases, the smallest values probably correspond to the true concentration in the solid solution. The higher

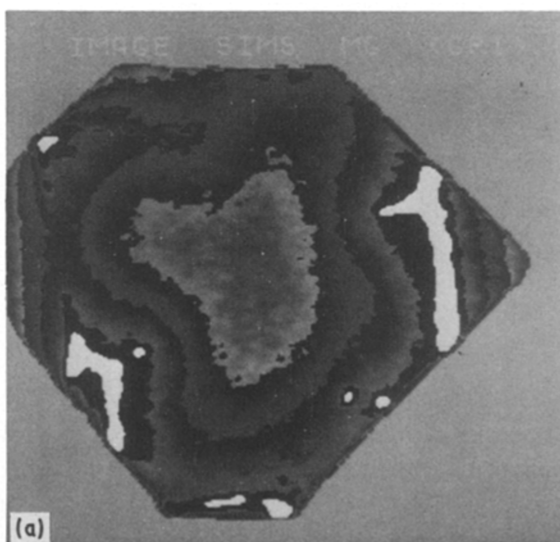

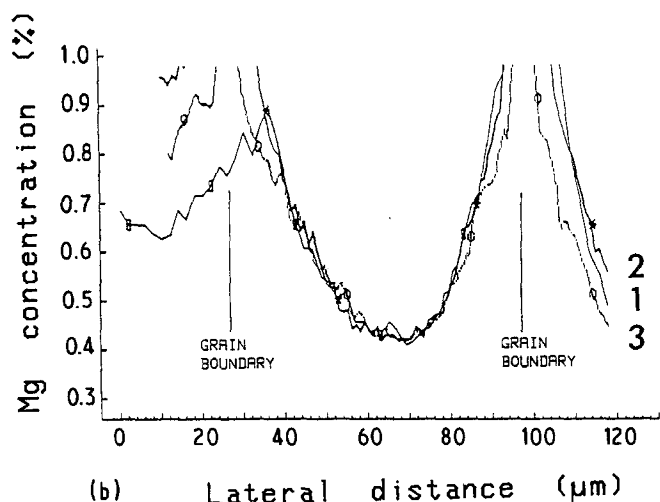

Figure 18 (a) Normalized and calibrated $^{24}Mg^+/^{27}Al^+$ ion micrograph resulting in a quantitative magnesium concentration map in an Al–Li–Mg–Cu as-cast alloy. (b) Comparison of quantitative lateral scans of the magnesium concentration within the same grain as (a) using three different techniques: (1) EPMA, (2) SIMS lateral "step scan" and (3) lateral pixel scan obtained from the image (a) using an image analyser [23]. Ar^+ bombardment at 8 keV with O_2 flooding.

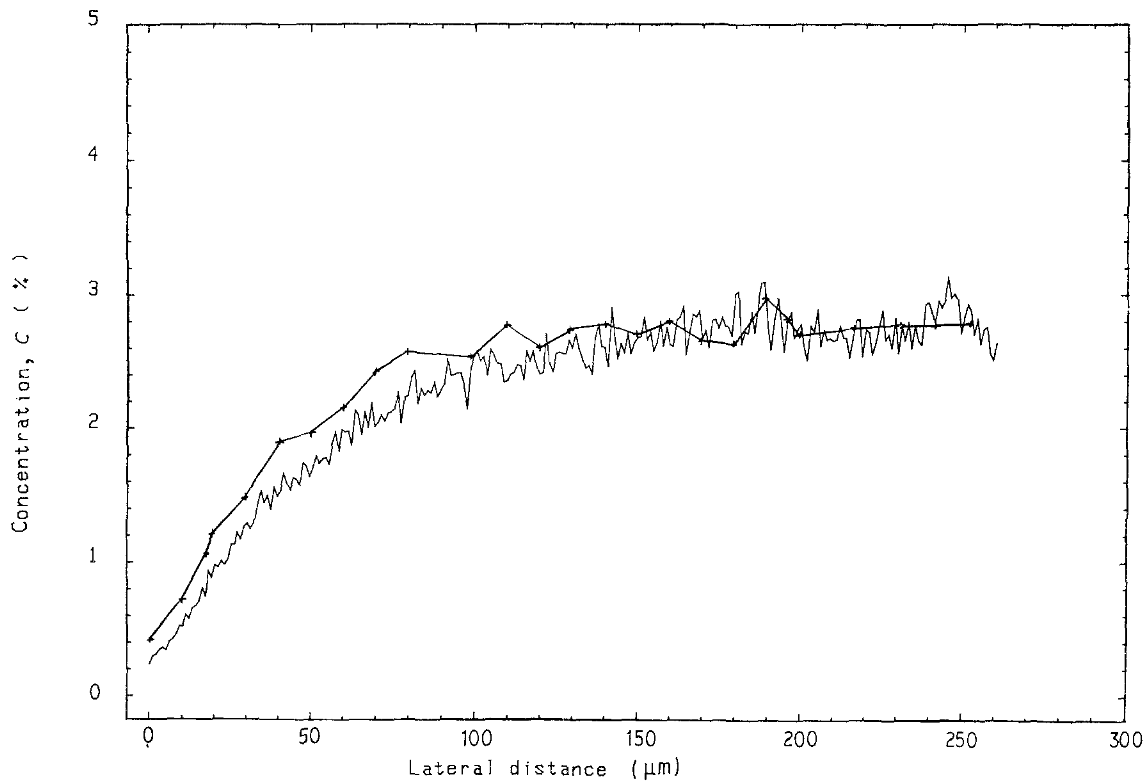

Figure 19 Comparison of lateral line scans of the lithium concentration across the thickness of a sheet of heat-treated Al–Li (2.8% Li) alloy by two different techniques. (——) SIMS, Ar^+ (8 keV) + O_2; (+) nuclear microprobe [45], ^7Li (p, α) ^4He.

values correspond to various contributions from iron-rich phases on and underneath the surface. The SIMS analysis in phase-free areas (pre-selected using iron ion micrographs), using a single external standard, gave well-defined values of 37 ± 3 and 101 ± 10 $\mu g\, g^{-1}$, respectively. In each case, these discrete values correspond to the leading edge of the EPMA histogram. It may be concluded that the heat treatment at higher temperature leads to nearly total dissolution of iron, since the concentration in the solid solution is not significantly different from the bulk concentration.

A further example illustrating the quantitative

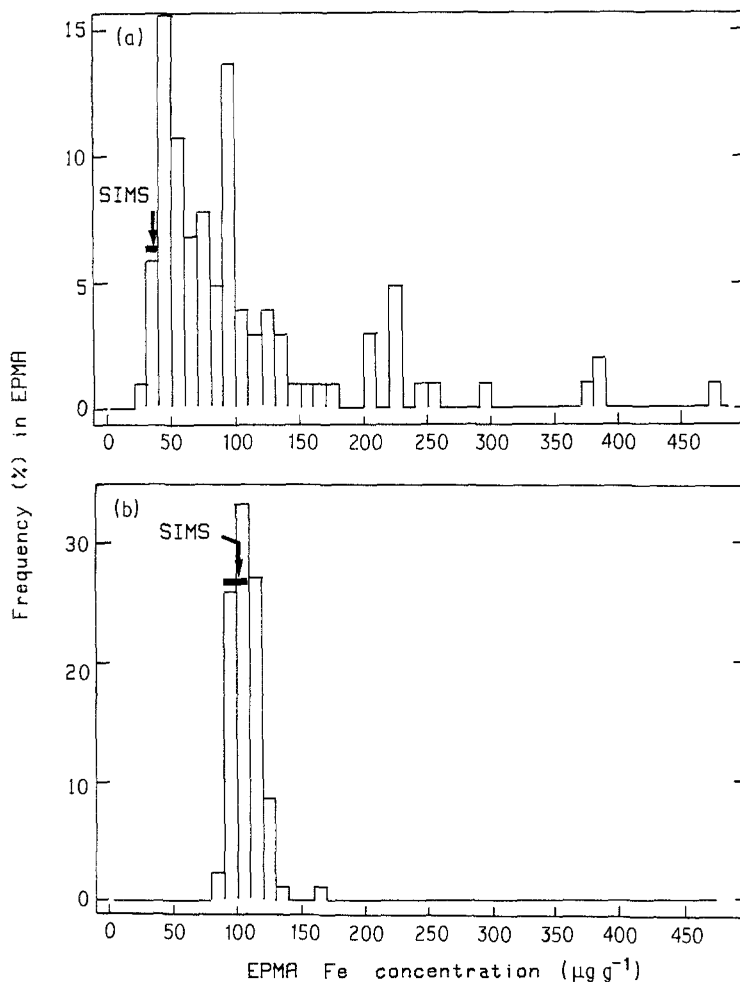

Figure 20 Histograms of local concentration given by EPMA in a 7X75 (Al–Zn) aluminium sample containing iron at 105 ± 8 $\mu m\, g^{-1}$ for two heat treatments at (a) T_1 and (b) T_2 ($T_2 > T_1$). The SIMS values are well defined and correspond to the leading edges of the EPMA histograms.

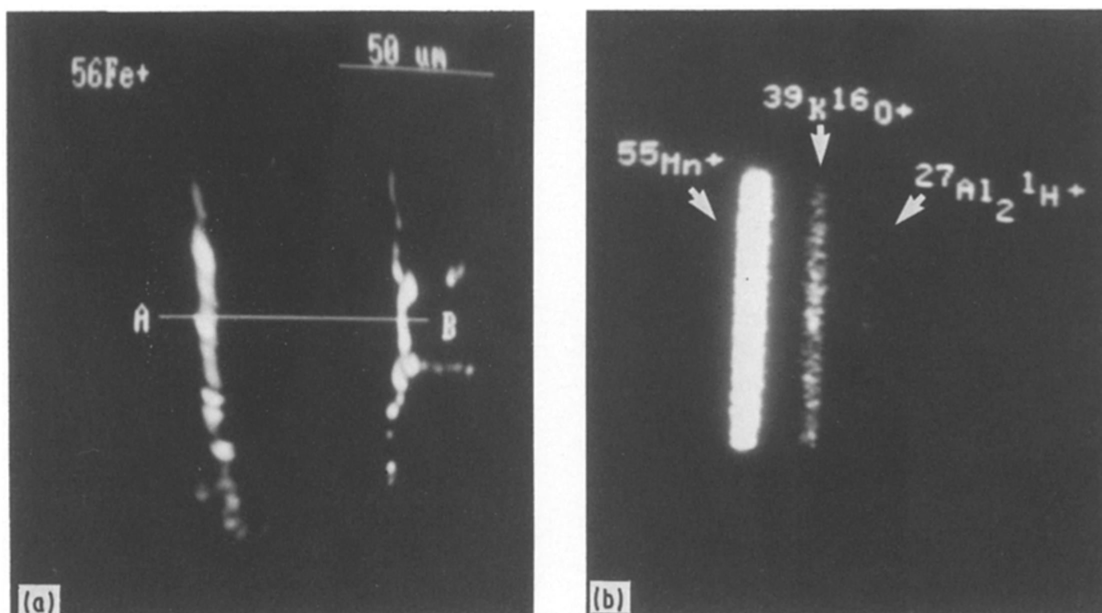

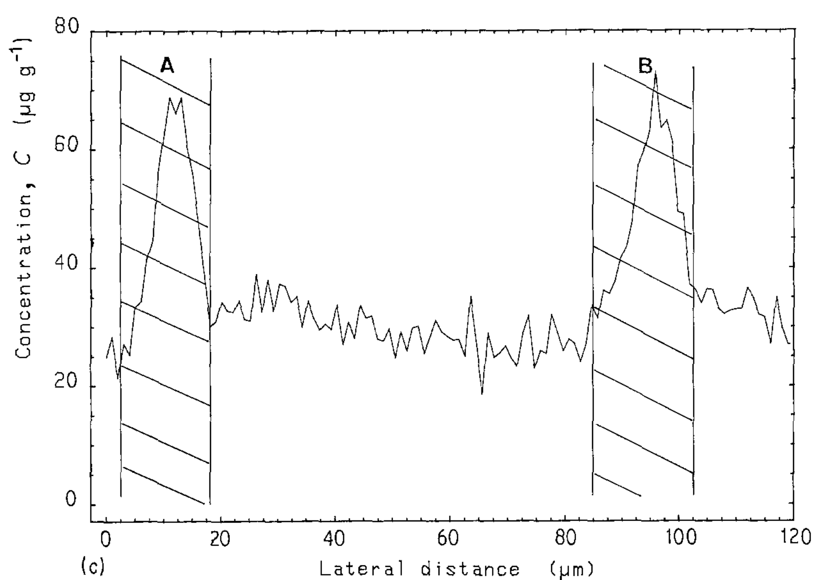

Figure 21 Line scan analysis with $1\,\mu m$ lateral resolution of manganese at low concentration within the solid solution of an aluminium alloy. (a) Iron-rich intermetallic phases decorate the grain boundary, facilitating selection of analysis zone. (b) Mass spectrographic spectrum showing three peaks at 55 daltons. Analysis of monoisotopic manganese ($^{55}Mn^+$) was performed at high mass resolution $M/\Delta M \approx 3000$). (c) Resultant lateral analysis showing a uniform manganese distribution of about $30\,\mu m\,g^{-1}$ within the selected grain. Each analysed point corresponds to a consumption of $\approx 10^{-13}$ g Al and $\approx 10^{-18}$ g Mn. O_2^+ bombardment at 8 keV.

microanalysis of low-concentration elements in the solid solution is given in Fig. 21 for an aluminium alloy (0.56% Fe, $50\,\mu g\,g^{-1}$ Mn). It was required to determine both the concentration and the lateral distribution of mangenese within grains of about $50\,\mu m$ diameter. The $^{56}Fe^+$ ion micrograph of Fig. 21a was obtained from a polished cross-section of the alloy and revealed iron-rich intermetallic phases which decorate the grain boundaries. From this micrograph, the lateral scan A $\rightarrow$ B traversing a grain was selected. A lateral line-scan analysis was performed by displacing an analysis zone of $\approx 1\,\mu m^2$, in steps of $1\,\mu m$, from A to B. At each point, a layer of about 100 nm of material was sputtered (corresponding to 3×10^{-13} g Al) to obtain a statistically significant $^{55}Mn^+$ signal (4 total c.p.s.).

An additional complication was the presence of the interference peaks KO^+ and Al_2H^+ at 55 daltons. As manganese is monoisotopic a mass resolution of $M/\Delta M \approx 3000$ was needed to perform correctly the analysis (Fig. 21b). The resultant quantitative line-scan is shown in Fig. 21c, indicating a uniform manganese concentration of about $30\,\mu g\,g^{-1}$. The calibration in concentration was performed using an external reference sample. Note that the absolute quantity of manganese consumed for each data point (analysis containing $30\,\mu g\,g^{-1}$ Mn) corresponds to about 10^{-18} g or to 10 000 manganese atoms. In addition it is necessary to point out that the shaded regions correspond to the grain-boundary intermetallic phases, and due to matrix effects in SIMS (Section 2.6) the concentration scale is not valid.

By integrating ion signals in a larger but homogeneous sputtered volume (up to $10^{-8}\,cm^{-3}$), trace and ultra-trace analysis down to the p.p.b. level can be performed [34].

Quantitative analysis using an external standard yields an accuracy of better than 25% relative (generally 10%).

5.2. Phases, small precipitates

Due to matrix effects at high concentration ($C > 1\%$) a quantitative analysis requires careful calibration with standard compounds of composition similar to

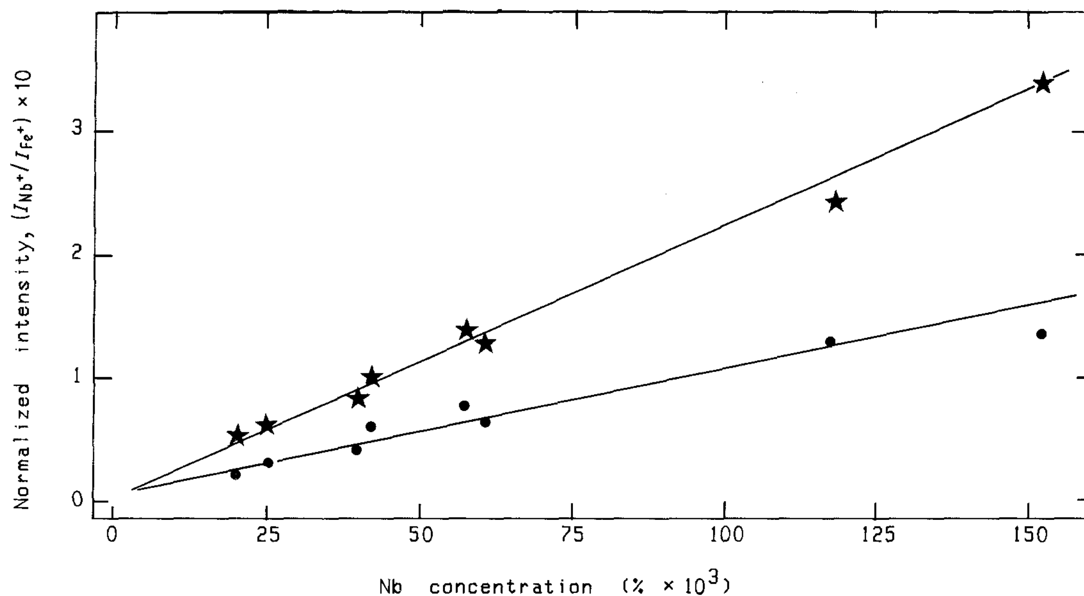

Figure 22 Normalized Nb^+/Fe^+ intensity against the bulk niobium concentration for two precipitation states of niobium in an iron matrix; (●) true solid solution and (∗) NbC precipitates [49].

the phase to be identified. Paradoxically, quantitative analysis is harder to perform in SIMS when the concentration increases. Once again, EPMA, and more recently NM [47] and SAM, can be used as reference techniques to determine the content of major elements in phases.

When the dimension of the phase exceeds the lateral resolving power of the SIMS instrument, direct characterization is possible. For instance, Pivin *et al.* [48] could establish the stoichiometry of complex oxides of chromium and nickel from the relative intensities of selected atomic and molecular ions.

When the size of the precipitates is smaller than the lateral resolving power, it is impossible to select them for individual characterization and the ion signal I includes a contribution from the matrix and from the precipitates, as in Fig. 17a. Nevertheless, it is still possible under certain conditions to deduce *average* information about the precipitation state. For instance, Namdar *et al.* [49] could estimate a precipitation rate for the fine phases AlN and NbC present at small concentrations in steel by monitoring the normalized intensties. I_{Al^+}/I_{Fe^+} and I_{Nb^+}/I_{Fe^+} with respect to the global concentration of aluminium and niobium, respectively. The variation was linear for both a pure true solid-solution state and for a totally precipitated state, but the slopes were different (Fig. 22).

In summary, quantification in metallurgical samples is at best delicate. However, in many cases, suitable standard samples of similar microstructure are available or can be prepared. Hence, SIMS can provide local quantitative microanalysis, rather easily for high and low concentration in the solid solution/matrix and with more difficulty within phases.

6. Surface, thin film and interface analysis by depth profiles

For heterogeneous structures in depth, the position of the subsurface(s) with respect to the initial sample surface is of prime importance since this later defines the position of the erosion plane (Fig. 23). When the subsurface interfaces are naturally parallel (Fig. 23a)

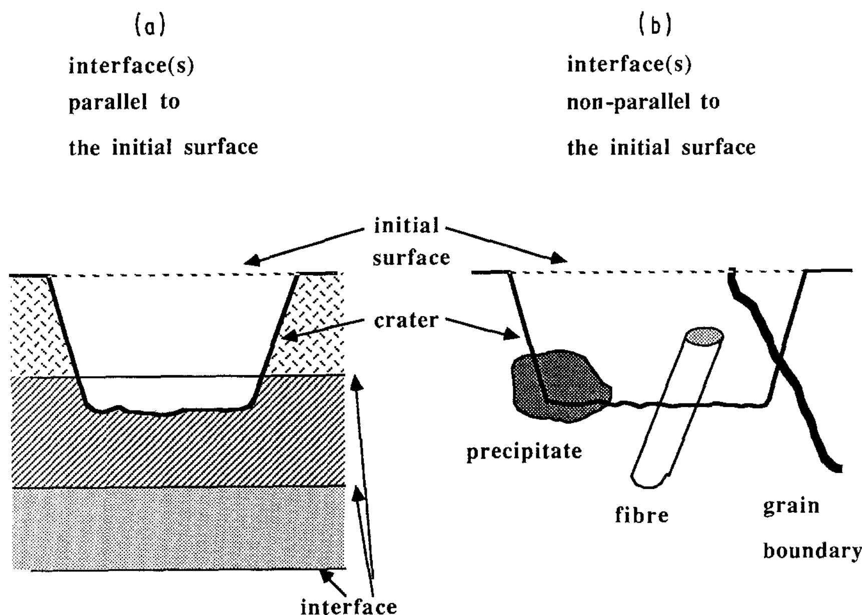

Figure 23 Schematic representation of the two sample configurations for in-depth analysis: interface(s) (a) parallel and (b) non-parallel to the initial sample surface.

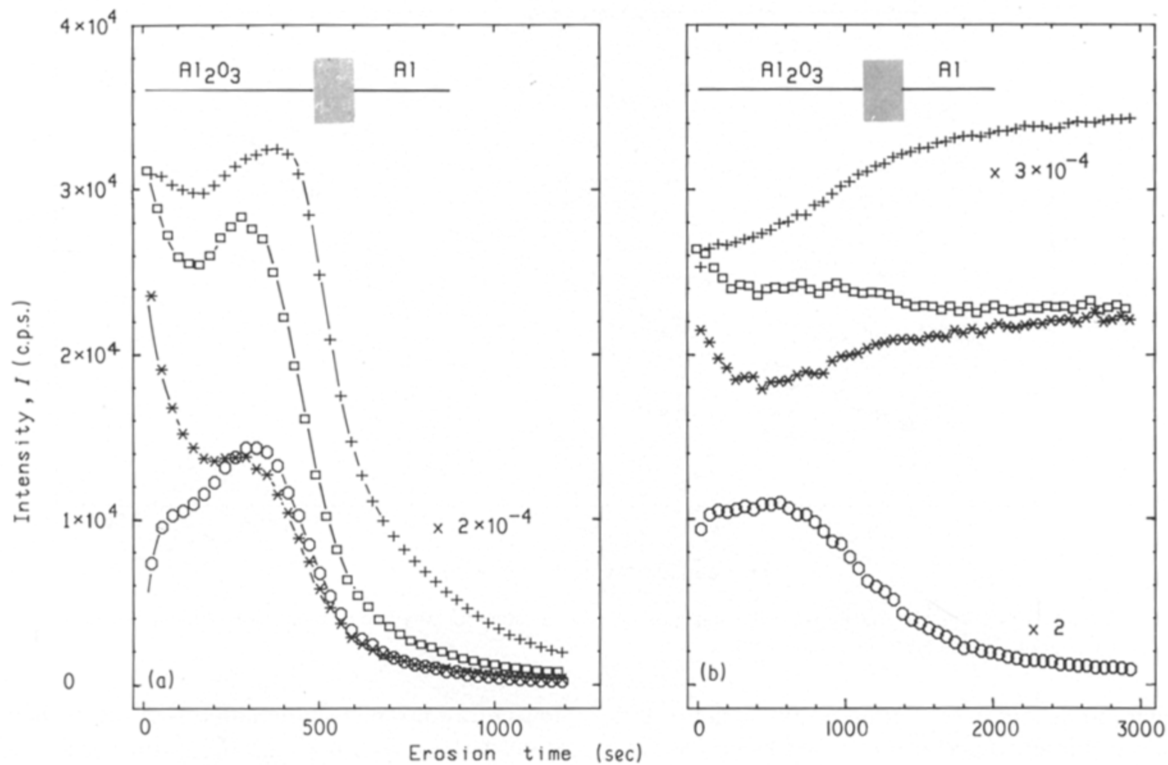

Figure 24 Depth profiles of the major elements for an aluminium sheet covered by a 7.0 ± 0.5 nm oxide layer enriched in ^{18}O. (a) Ar^+ bombardment at 8 keV, (b) influence of O_2 flooding [32]. (+) $^{27}Al^+$, (*) $^{16}O^+$, (○) $^{18}O^+$, (□) $^{16}O^+$ + $^{18}O^+$.

to the initial surface (oxide layer, multilayered thin films, deposited film for diffusion studies etc.) the sample can be analysed "as-received". When randomly oriented (precipitate–matrix, matrix–fibre, grain boundaries, etc.) (Fig. 23b), these subsurface interface(s) have to be preoriented and sample preparation is necessary.

6.1. Parallel interface(s)

6.1.1. Thin oxide layers

The composition and the structure of the several nanometre thick oxide layers which cover metals play a primordial role in the technological properties of these materials: protection, adhesion, corrosion, wear, vacuum brazing, etc. Such oxide layers have been investigated by SIMS [32, 50–53] in combination with other surface analytical techniques like Auger electron spectroscopy (AES), XPS and ISS.

Considerable matrix effects due to abrupt variations of sputtering yield and ionization probability (cf. Equation 1) arise in the oxide–metal interfacial region, as shown for the major elements $^{27}Al^+$ and $^{16}O^+$ in Fig. 24a for an aluminium sample [32]. Such analytical artifacts causing a distortion of the real profiles (aluminium for instance) can be minimized [20] by flooding oxygen to saturate the surface, thus imposing a quasi-constant oxide stoichiometry (intensity of major elements $^{27}Al^+$ and $^{16}O^+$ nearly constant in Figs 7 and 24b). This assumption was checked by the ESCA analysis of a natural oxide layer and of an Ar^+ sputtered cleaned aluminium surface oxidized in an oxygen atmosphere. In the case of Figs 24 and 25 ^{18}O was introduced as an isotope tracer in the atmosphere during the oxidation of aluminium at 425° C. The $^{18}O^+$ secondary ion permitted the location of the oxide–metal interface in the experimental depth profile $I(t)$ by the transition time t_t necessary to reach a 50% reduction of the maximum intensity (Figs 24a and b). In this way, it was observed that beryllium and magnesium impurities were present at the oxide–metal interface (Fig. 25). Their transition times vary linearly (Fig. 26) with the oxide thickness between 3.5 and

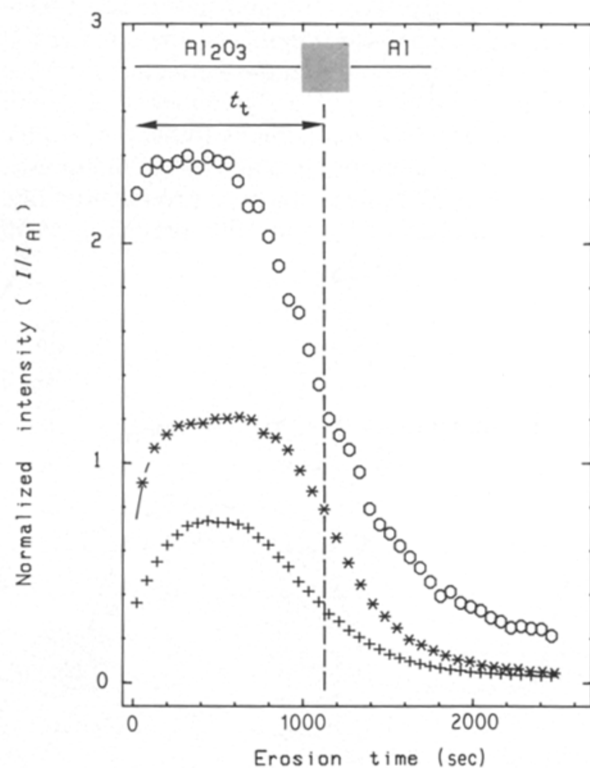

Figure 25 Normalized depth profiles of the major element ^{18}O and of the segregated impurities ^{9}Be and ^{25}Mg for an aluminium sheet covered by a 7.0 ± 0.5 nm oxide layer enriched in ^{18}O [32]. (○) $^{18}O^+$ (×4 × 10^4), (+) $^{9}Be^+$ (×6 × 10^2), (*) $^{25}Mg^+$ (×6 × 10^2).

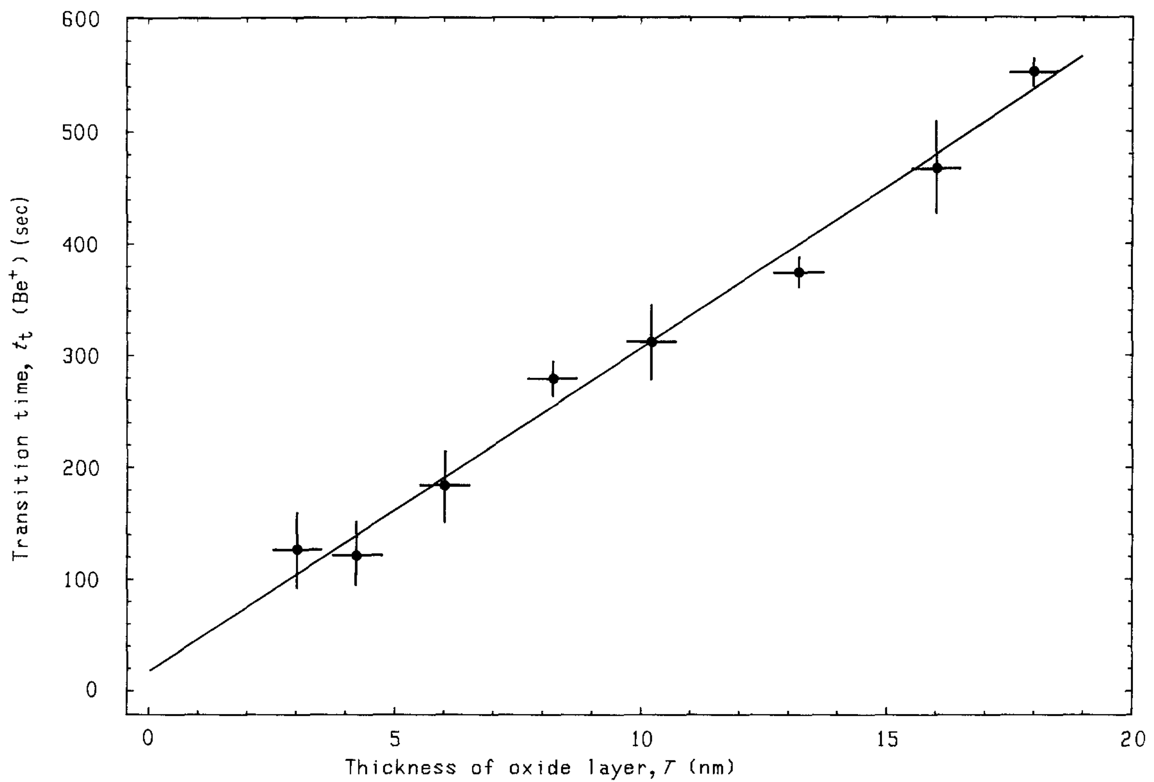

Figure 26 Variation of the transition time t_t (Be^+) necessary to reach a 50% reduction in the tail at greater depth with respect to the oxide layer thickness measured by ellipsometry [32]. Ar^+ (8 keV) + O_2.

18 nm as measured by ellipsometry. Conversely, the transition time may be used to determine the oxide thickness of an unknown sample.

With optimal operating conditions (sputtering at low energy, high incidence angle and O_2 flooding), unique quantitative information on the three-dimensional distribution of major and (unexpected) minor elements can be obtained at the surface of the oxide, within the oxide, at the oxide–metal interface and within the metal bulk. The depth profiles in Fig. 27 illustrate the tremendous surface enrichment (10^3 to 10^4) of alkaline (lithium, sodium) and alkaline-earth (beryllium, magnesium) impurities with respect to the bulk observed in a heat-treated polycrystalline

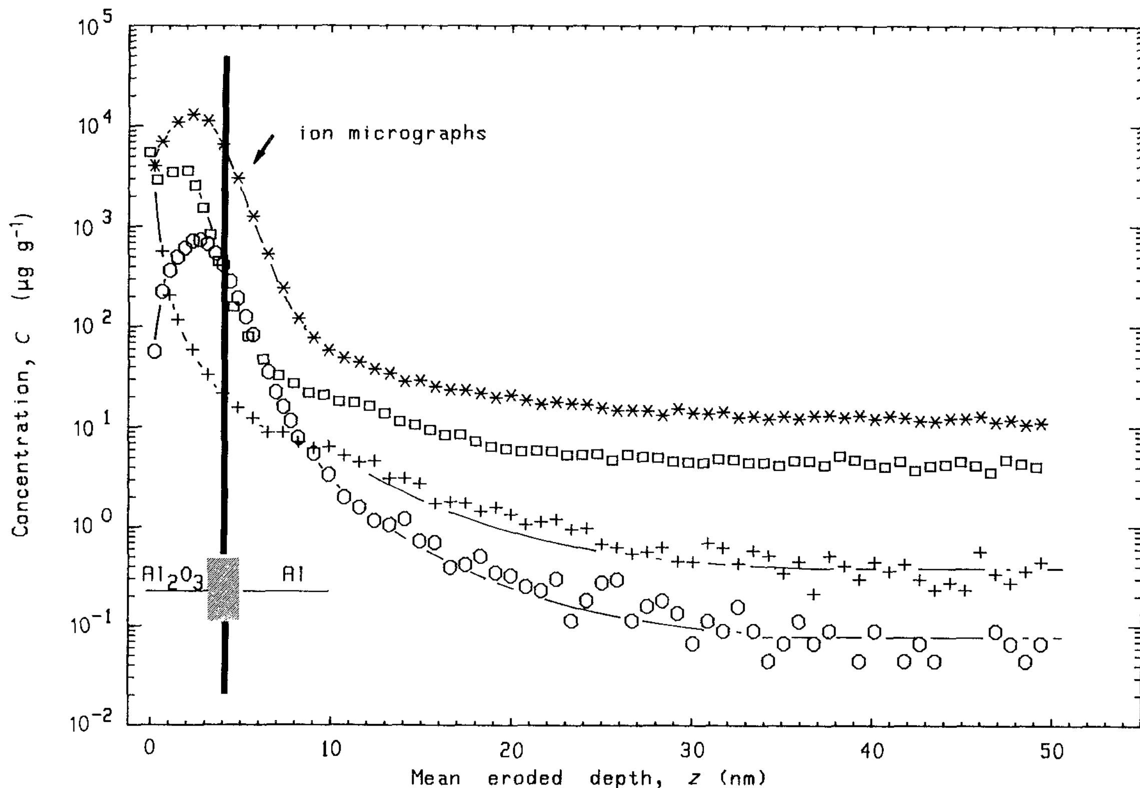

Figure 27 Depth profile of segregated impurities (+) lithium, (□) sodium, (○) beryllium and (*) magnesium for an aluminium sheet covered by a 4.2 ± 0.05 nm oxide layer. The arrow indicates the region where the ion micrographs of Fig. 13 were recorded [32]. Ar^+ (2.5 keV) + O_2.

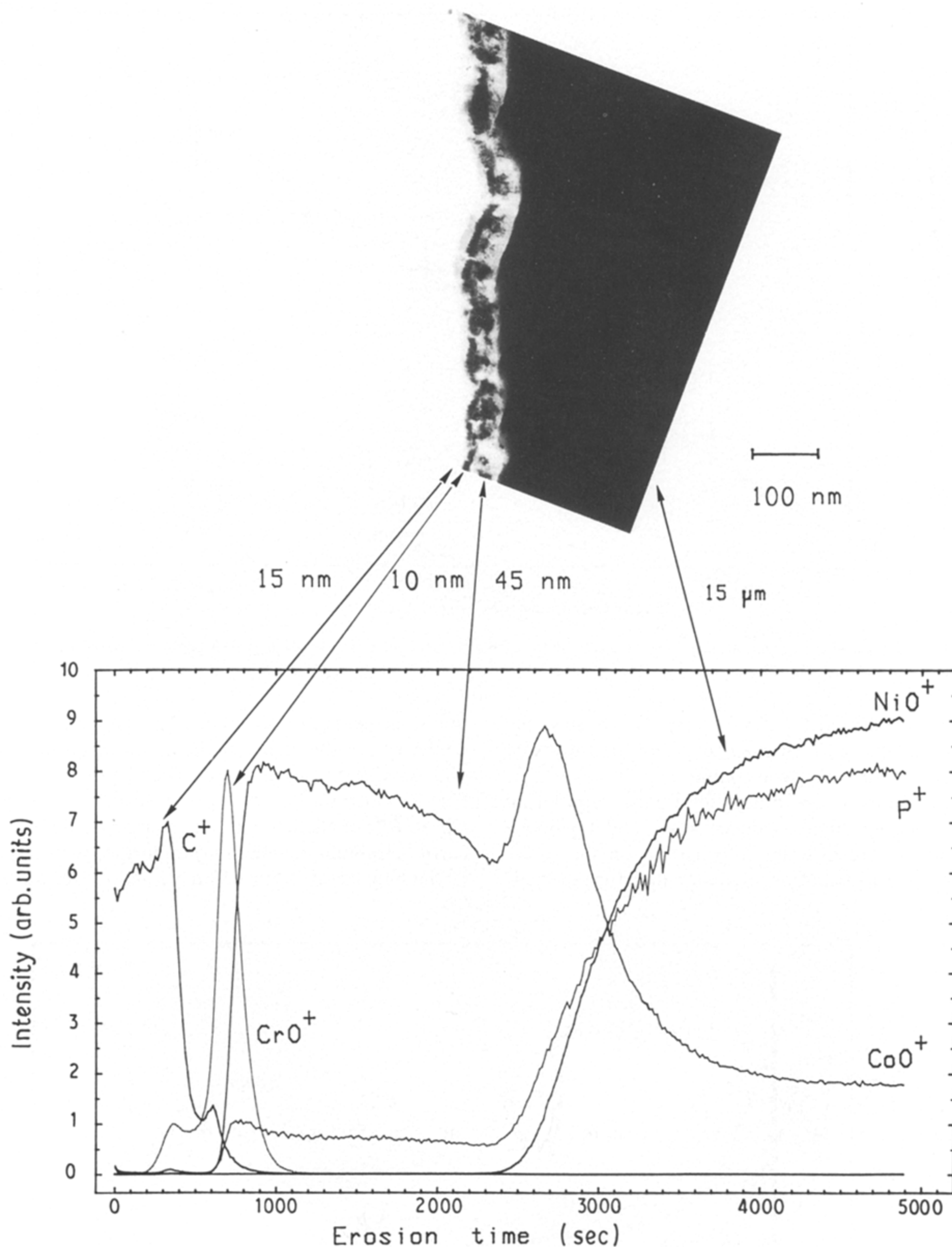

Figure 28 Top: transmission electron micrograph at high magnification (≈ 100 000) of an ultramicrotomed section of three successive thin layers of carbon, chromium and cobalt on a thick Ni–P layer deposited on an aluminium substrate. Bottom: depth profiles of characteristic ions of these layers. Ar^+ bombardment at 2.5 keV with O_2 flooding.

aluminium sheet [32]. Lithium and sodium tend to be more concentrated at the uppermost surface (air–oxide interface) and play an important role in the adhesion of polymer films [52], while beryllium and magnesium are more concentrated at the oxide–metal interface. Ion micrographs taken just below the oxide–metal interface show (cf. Fig. 13) that beryllium, and to a lesser extent sodium, partially segregate to the surface via a grain boundary diffusion mechanism, while the distributions of lithium and magnesium are not correlated with the grain boundaries. Once again, note that such information could not be obtained by the conventional surface techniques like ESCA and SAM due to their relatively poor detection limit and the nature of the high dynamic concentration profile.

6.1.2. Multilayered films

The rapid succession of different matrices make the calibration of both depth and composition difficult. Complementary data can be given by TEM/STEM on cross-sections prepared by ultramicrotomy [54]. Slices of material, typically 50 nm thick and cut

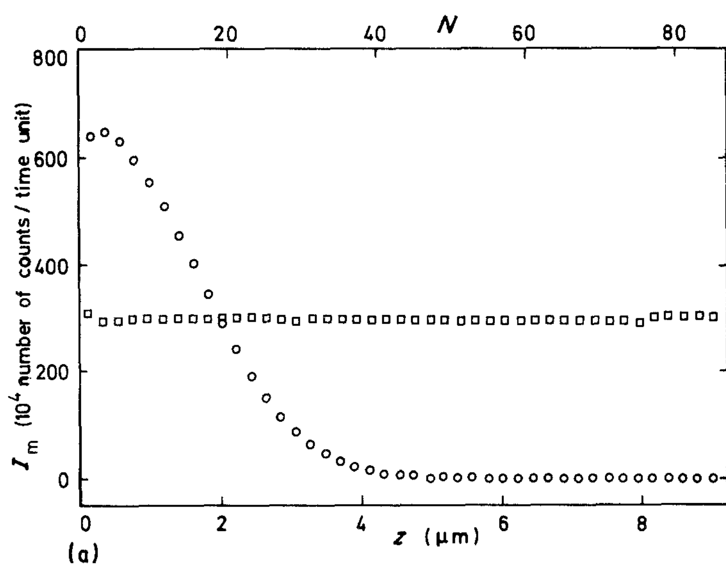

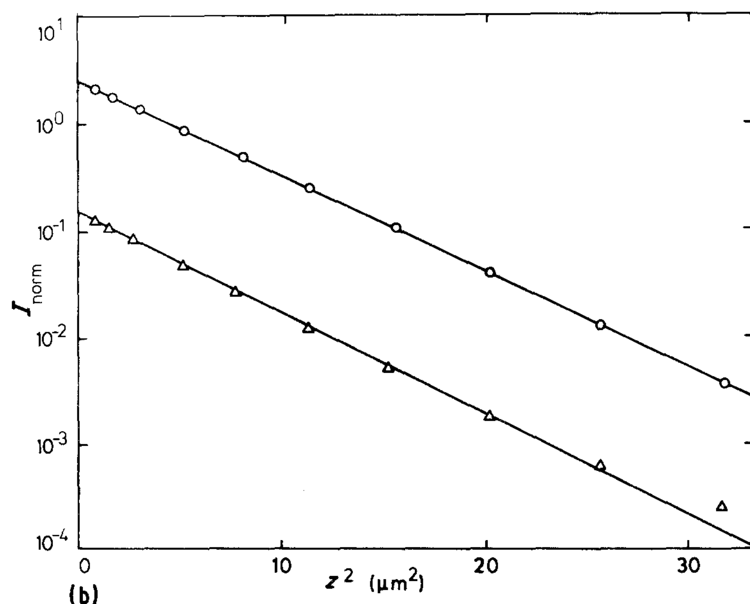

Figure 29 (a) Depth profile of indium diffused in monocrystalline copper showing a plot of $^{115}In^+$ intensity I against depth and (b) log $I(In^+)$ against z^2, the slope giving the diffusion coefficient D [55]. (○) $^{115}In^+$, (□) $^{65}Cu^+$, (△) $^{113}In^+$.

perpendicularly to the interface are investigated in the TEM mode at high magnification (up to 300 000) to display the size and the morphology of the layer(s).

Positioning an electron nanoprobe (several nanometres in diameter) in the STEM mode gives local X-ray semi-quantitative chemical analysis for major elements and allows electron diffraction studies. Fig. 28 illustrates the interest of combining SIMS depth profiles with TEM micrographs at a magnification of $\approx 100\,000$ for the characterization of three successive layers of carbon (15 nm), chromium (10 nm) and cobalt (45 nm) on a thick layer (15 µm) of nickel (containing phosphorus) deposited on the aluminium substrate of a computer disc.

6.1.3. Bulk diffusion

Diffusion is a key mechanism for solid-state transformation and the experimental diffusion coefficient D is of prime importance to understand and predict metallurgical phenomena. The distance z concerned in *unidirectional* diffusion can be estimated by $z = 2(Dt)^{1/2}$ where t is the heat treatment time at a given temperature. If the diffusing element is deposited as a pure thin layer (10 to 30 nm), on [55] or within [56] the substrate prior to the heat treatment, its depth profile provides the quantitative variation of the concentration with z. Due to the excellent resolution in depth (several nanometres), SIMS was able to furnish the lowest experimental values of D (in the 10^{-19} cm^2 sec^{-1} range) [57]. Fig. 29a shows the results obtained by Gust *et al.* [55] for the depth profile of indium diffused in monocrystalline copper, and Fig. 29b the direct determination of D from the slope of the reprocessed log I against z^2 line. Note that the identical lines observed for the two isotopes 113 and 115 of indium are shifted by the correct isotopic abundance ratio. This gives increased confidence in the capabilities of SIMS for the determination of diffusion coefficients.

6.1.4. Organic thin films on metallic substrates

For deposited films in the monolayer or sub-monolayer range, the thickness is rather implicitly defined (between 0.3 and 1 nm) but the lateral distribution may be heterogeneous. A depth profile would not present a sharp transition at the interface and would not be practically exploitable.

The following example concerns an aluminium sample having an average of only a few monolayers of a silane molecule deposited on its surface. In adhesive

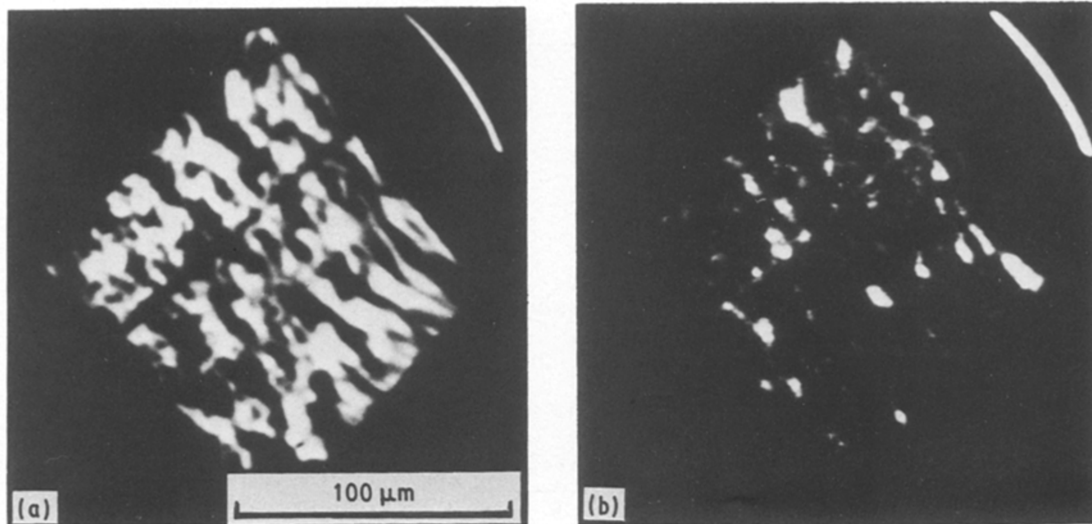

Figure 30 Ion imaging of a thin organic surface film as illustrated by an aluminium sample covered with a silane layer several monolayers (average) thick. (a) The substrate as revealed by the $^{27}Al^+$ image (averaged 6 sec); (b) the $^{45}SiOH^+$ molecular ion image (averaged 55 sec), confirming the heterogeneous silane distribution. Ar^+ bombardment at 2.5 keV [23].

bonding silane increases the bond strength by acting as a bridge between the surface oxide and subsequently applied adhesives or polymer films. After obtaining mass spectra under low-energy bombardment (Ar^+, 2.5 keV) with a total dose of 10^{12} ions cm^{-2} it was found that the $^{28}Si^{16}O^1H^+$ molecular ion at 45 daltons could be used as characteristic of the silane molecule.

Molecular ion micrographs [23] were obtained using a current density of 10^{15} ions cm^{-2} sec^{-1} using image integration techniques, which corresponded to a total does of 5×10^{16} ions cm^{-2}. Fig. 30a shows the

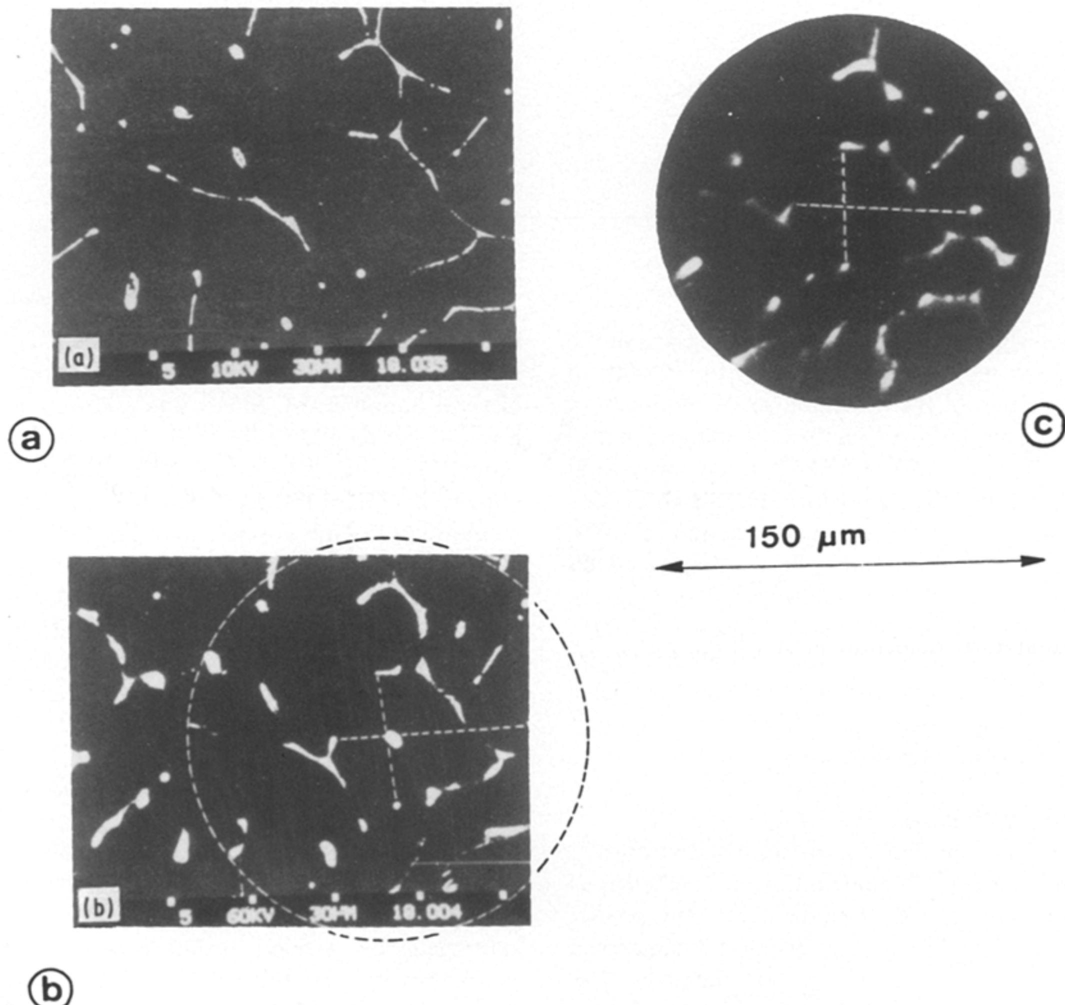

Figure 31 Triangulation procedure to locate sub-surface phases by combining SEM and SIMS. (a, b) SEM images of back-scattered electrons at 10 and 60 keV, respectively, allowing the location at the intersection of the two dotted segments of a phase under the surface; (c) SIMS Fe^+ ion image (1 sec) of the same area and localization of the underlying phase. O_2^+ bombardment at 8 keV [58].

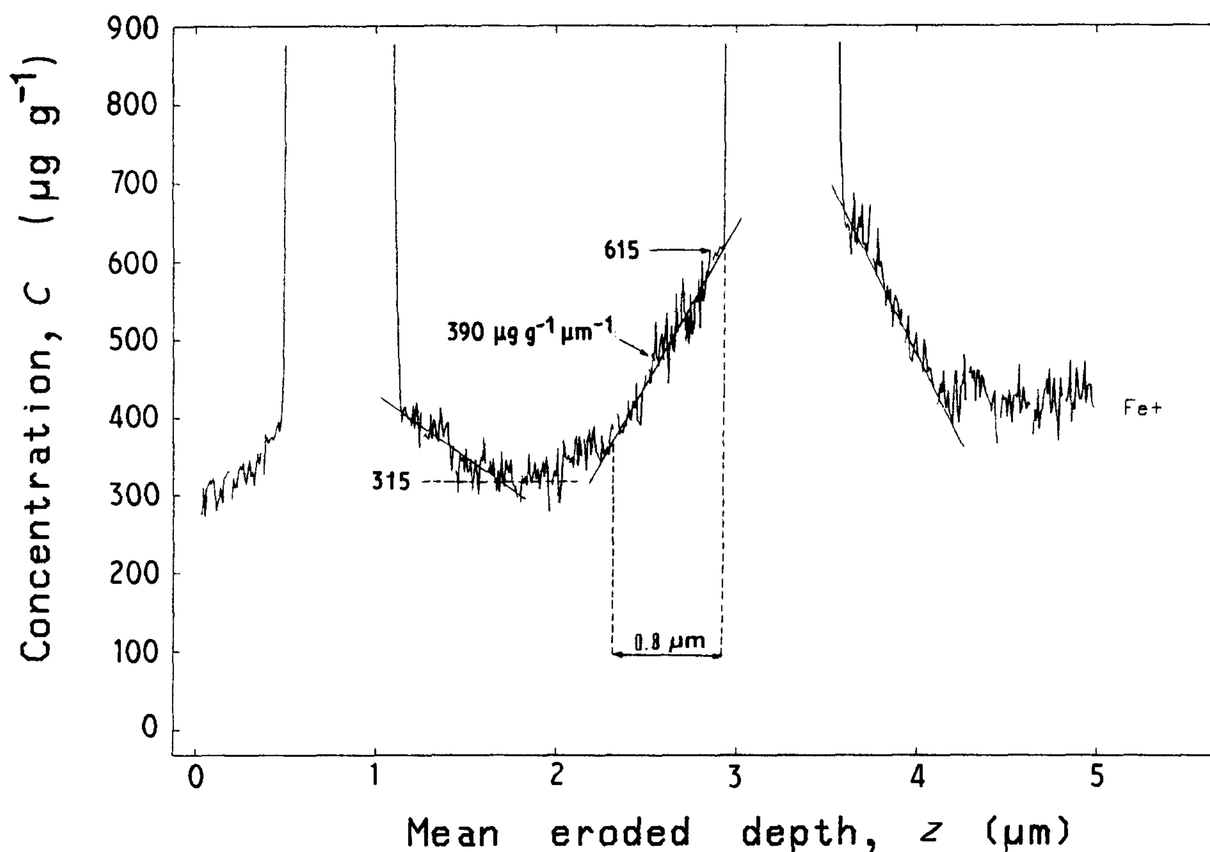

Figure 32 Depth profiles of iron after pre-location (Fig. 31). The concentration scale was calibrated with a single standard sample containing iron in solid solution and the eroded depth scale was calibrated with a profilometer. O_2^+ bombardment at 8 keV [58].

Al^+ image revealing areas of the substrate aluminium surface oxide. The dark regions correspond to the silane surface distribution as seen by the $SiOH^+$ ion micrograph of Fig. 30b. For the particular application process employed, it can be concluded that the silane was not uniformly distributed on the microscale. SIMS may be combined with more conventional techniques like ESCA or infrared spectroscopy to provide the necessary chemical and spatial information.

6.2. Randomly oriented interface(s)

6.2.1. Concentration profile at a matrix–precipitate interface

Alloys in the as-solidified state usually exhibit a segregated structure: for instance, a concentration profile of minor elements in the solid solution between two interdendritic areas, and especially very close to intermetallic phases. High spatial resolution (< 10 nm) and low analytical detection limit ($< 10\,\mu g\,g^{-1}$) are necessary to record such concentration profiles. Complementary use of SEM and SIMS can resolve the problem as illustrated in the following example [58]. In the SEM, sub-surface micrometre-sized iron-rich precipitates were first located in an aluminium matrix by comparison between two back-scattered electron images obtained at different primary energies (10 to 60 keV) (Figs 31a and b), i.e. with information coming from different depths. These micrographs, and in particular the most surface-sensitive one obtained at low energy, were then correlated with the surface Fe^+ ion micrograph of the same area (Fig. 31c). A triangulation procedure allowed the precise location in the SIMS instrument of a precipitate actually below the surface (0.5 to 1 µm). Finally, depth profiles on this small area (8 µm in diameter) showed a significant enrichment of iron in the solid solution ($300\,\mu g\,g^{-1}$) near intermetallic Al–Fe phases (Fig. 32). In addition, the profile shape could be quantitatively interpreted by a theoretical solidification model [59].

In principle, the total procedure involving first the pre-location and then the depth profile could now be replaced by so-called "retrospective" depth profiles [60]. Digitized ion micrographs obtained at different depths are stored in an image analyser and reprocessed *a posteriori*. The coördinates of a zone of interest are obtained from an image at a depth where the erosion front intersects a phase. Depth profiles are recorded by taking the grey level or count rate at the selected area in each of the stored images.

6.2.2. Segregation at grain boundaries

Segregation of minor impurities at the grain boundary can modify drastically the macroscopic mechanical properties of a metal [61]. In recent years SAM has provided unique information on this mechanism by the analysis of fracture surfaces prepared in an ultra-high vacuum. However, SAM presents two limitations: the sample must necessarily present an intergranular fracture mode and the detection limit on any surface is around 1 at %. In favourable cases, i.e. when the grain-boundary planes can be pre-located on metallographic cross-sections, SIMS can investigate the segregation of minor elements at grain boundaries on specially prepared samples, independently of their fracture mode. For instance, in rolled industrial alloys, the grains may be very thin, flat, elongated

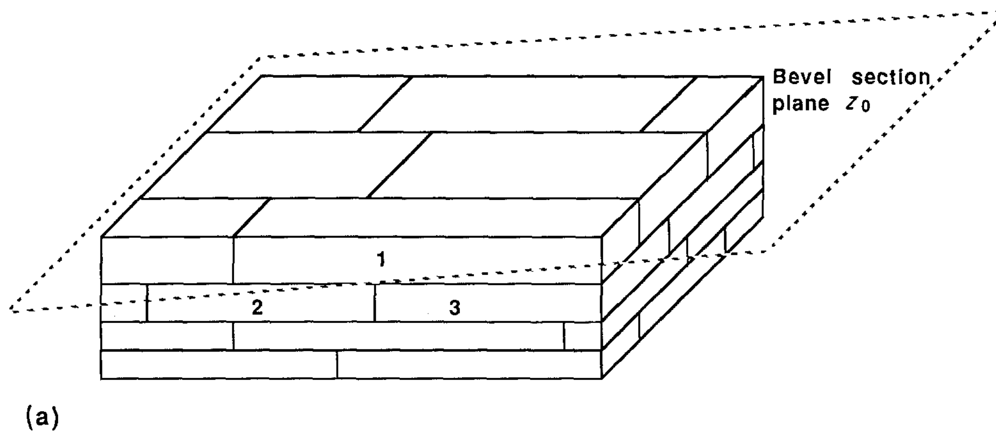

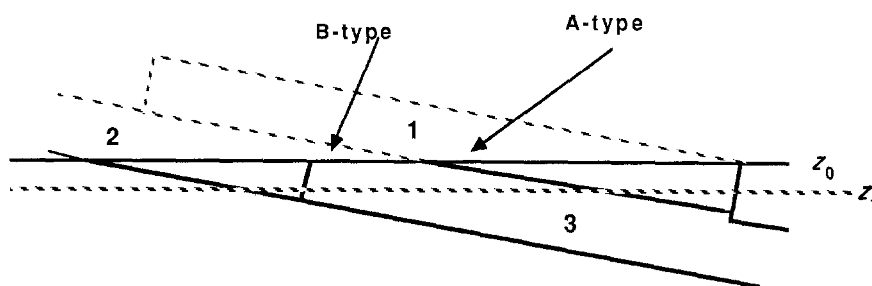

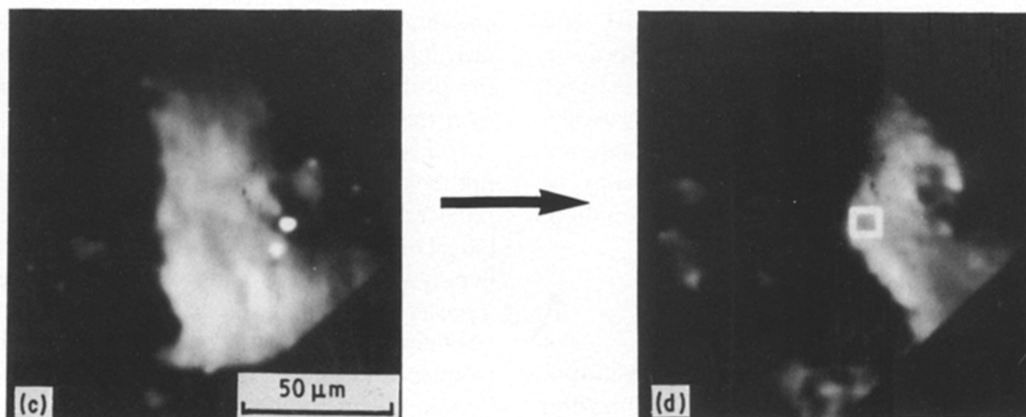

Figure 33 Schematic diagrams of (a) a sample with flat and elongated grains and (b) a low-angle bevelled section for investigation by depth profiling of segregated impurities at the grain boundary. (c) Ion micrographs of the Al^+ matrix ion at the initial stage of ion bombardment; the crystallographic contrast reveals two grains at an A-type boundary. (d) The same zone after several minutes of ion etching; the bright grain has receded towards the right of the image confirming that it is an A-type boundary. The black rectangle indicates the zone selected for SIMS depth profile analysis (cf. Fig. 34) [62]. Ar^+ bombardment at 8 keV.

and parallel to the sample surface. A bevelled section nearly parallel to the surface, i.e. with a controlled angle of only a few degrees between the surface and section plane, will cross different grains with a precise geometry, as illustrated in the schematic diagram of Fig. 33a and b by Grains 1, 2, and 3. At a given depth z_0, the grain boundary between Grains 1 and 3 appears at Point A and between Grains 2 and 3 at Point B. In the (x, y) plane, ion micrographs of the matrix ion under noble gas bombardment reveal the grains and hence the grain boundary by the crystallographic contrast (Section 4). As the matrix is sputtered away ($z_0 \rightarrow z_1$), the grain boundary at A appears to "move" rapidly towards the right with time. The direction and speed of this displacement of the boundary at A allows us to anticipate a position

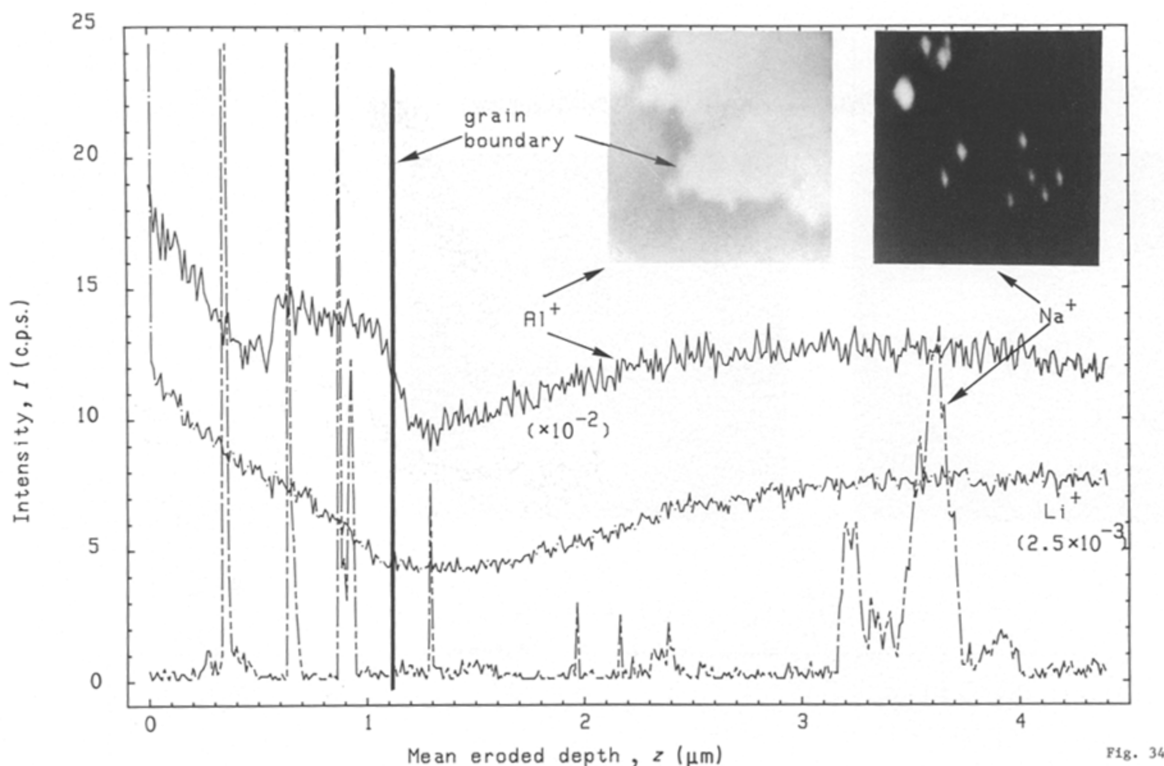

Figure 34 Depth profiles of aluminium, lithium and sodium at the grain boundary in a small diaphragmed region similar to that of Fig. 33d. An ion micrograph of the Na^+ impurity confirms a random distribution of small sodium-rich nodules (top right) [62]. Ar^+ (8 keV).

where it is certain that a grain boundary is only just beneath the surface; depth profiles can be carried out across the identified grain boundary on a small diaphragmed area (several square micrometres) to yield a good depth resolution. An example is given for an Al–Li alloy [62] in Figs 33c and d by the two Al^+ ion matrix micrographs. In this case the segregation of sodium, present in the bulk at several $\mu g\,g^{-1}$, appeared to be heterogeneous at the grain boundary (ion micrographs in Fig. 34, top right). The depth profile in Fig. 34 exhibits narrow peaks corresponding to sodium-rich nodules on each side of the grain boundary, the position of which may be located by the variation in the Al^+ intensity (crystallographic contrast). Note once again that the analysis was performed at high mass resolution ($M/\Delta M = 3000$) to distinguish from the monoisotopic ion $^{23}Na^+$ (22.9898 daltons) and the polyatomic matrix ion $^7Li^{16}O^+$ (23.0109 daltons).

Bevelled sections provide the added advantage that the section plane represents a magnified image of the depth scale. For instance, an interface region of $l = 200$ nm thick will appear as $x = 2\,\mu$m in the section plane using an $\alpha = 5.7°$ bevel section ($x = l$ cosec α). Mass spectra and ion images of thin interface regions become a reality (Section 6.2.3). It is expected that this procedure could be generalized for the study of trace-element segregation in various other industrial alloys.

By preparing well-characterized bicrystals, Gust *et al.* [63] could determine the grain-boundary diffusion coefficient of indium in copper and nickel. Depth profiles at different positions on a bevelled section were recorded for that purpose.

6.2.3. Enrichment at a matrix–fibre interface in a composite material

The preparation of bevelled sections as described in Section 6.2.2 can also be used for the chemical characterization of other interfaces, for instance between a metallic matrix and a fibre in a composite material. Fig. 35 presents an illustration of magnesium enrichment at the interface between the aluminium matrix and an SiC fibre in a composite material by the combination of ion micrographs and depth profiles.

In summary, providing that the microstructure is known by using other techniques (OM, SEM, TEM/STEM), depth profiles can provide unique information concerning concentration gradients on superficial layers, multilayered films and "internal surfaces" (grain boundaries, interfaces).

7. Use of isotopic tracers for mechanism studies

As the basic principle of SIMS consists in the detection of isotopes, isotopic tracers like ^{18}O, D_2, $D_2\,^{16}O$ and $H_2\,^{18}O$, incorporated during the sample treatment present a unique interest when studying chemical reaction mechanisms such as oxidation and corrosion processes. Thermal [32, 53, 64–66] and anodic [67, 68] oxidation of different metals have been investigated by using gaseous atmospheres or electrolytes enriched in specific isotopes of naturally low abundance.

For instance, in the characterization of thin oxide layers on aluminium (Figs 7 and 13), the oxide–metal interface could be unambiguously located in the depth profiles (Figs 24 and 25) by using the transition time of the $^{18}O^+$ ion corresponding to the tracer $^{18}O_2$ voluntarily introduced into the oxide layer. Conversely,

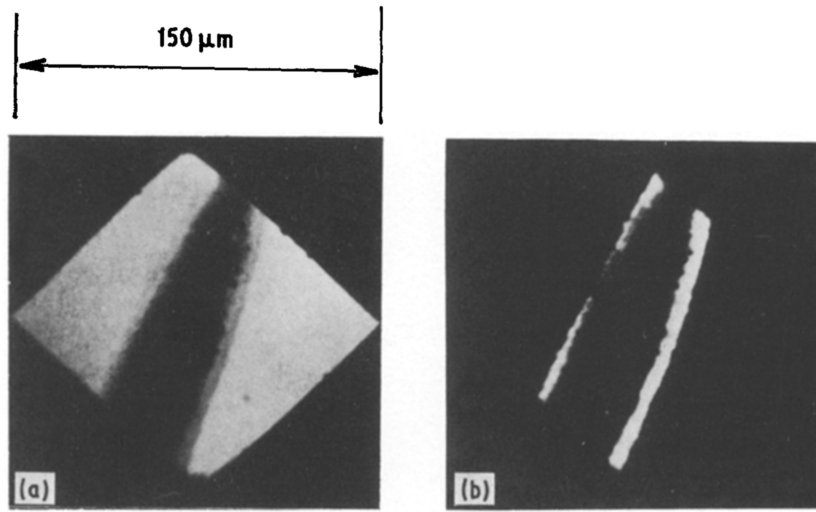

Figure 35 Analysis of a bevelled section at the interface between the aluminium matrix and an SiC fibre in a composite material. An enrichment in magnesium is observed in the ion micrographs for (a) $^{27}Al^{+}$, (b) $^{24}Mg^{+}$. (c) Depth profiles with O_2^+ (8 keV).

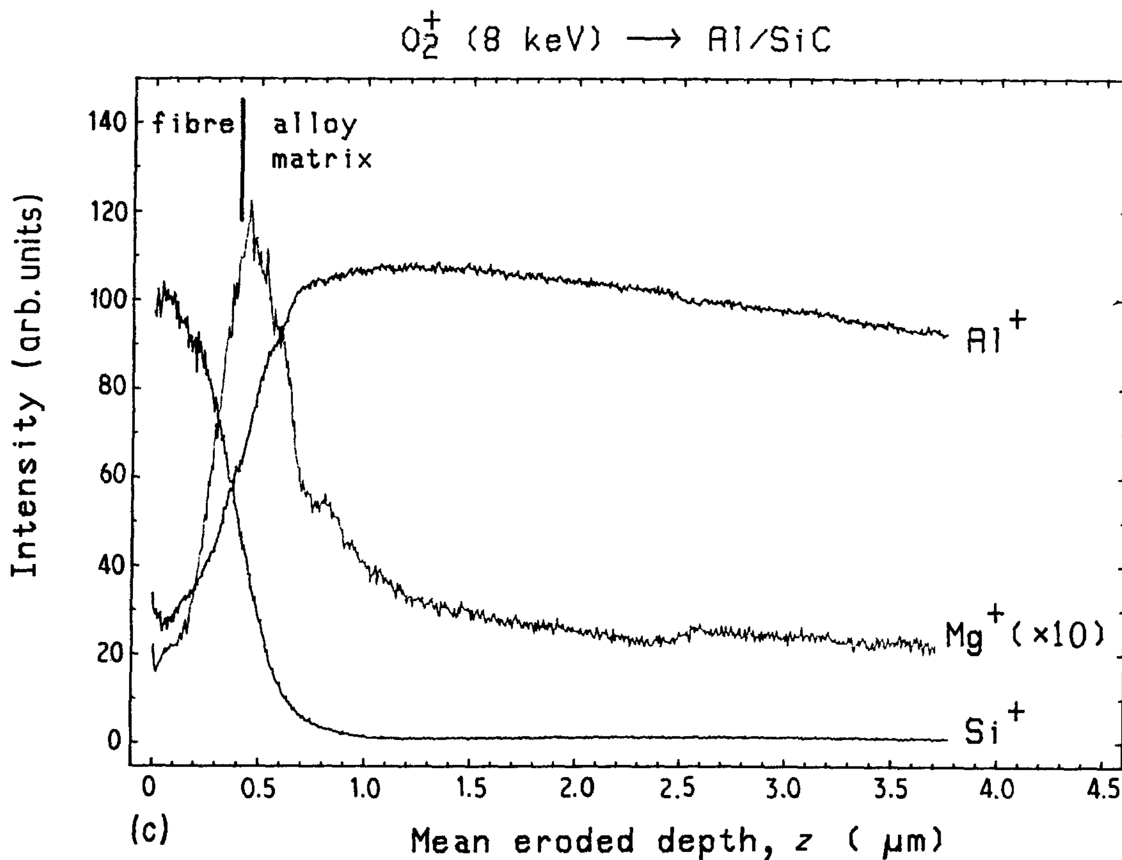

isotopic $^{18}O^{+}$ can be used primarily bombarding ion to study the distribution of ^{16}O in natural oxide layers (Fig. 36). In this case it is possible to separate the contribution of oxygen (^{16}O) naturally present and that (^{18}O) brought by the dynamic implantation process, their sum (^{16}O + ^{18}O) giving the total oxygen concentration at the surface which controls the emission of every ion and the hence the analytical result (cf. Section 2.3).

8. Conclusion

Due to its intrinsic properties (low detection limit and imaging capability of every element, depth resolution in the nanometre range), SIMS constitutes an original method for the characterization of heterogeneous metallic materials. Of prime importance is the complementarity between SIMS and the more conventional microscopic and microanalytical techniques. The analytical SIMS technique is capable of multimode operation, each mode being adapted to the diversity and polyvalence required in the domain of metallurgy and materials science research; this variety and interdependence of commonly employed SIMS operating modes is schematically illustrated in Fig. 37 [69].

Acknowledgements

The authors wish to thank Mrs Dussouillez, Mrs Madelan, Mrs Terroni and Mr Paillet for their technical assistance, Messrs Dubus and Dubost for their advice and Drs Demortier and F. Bodart for the novel application of the nuclear microprobe in metallurgy.

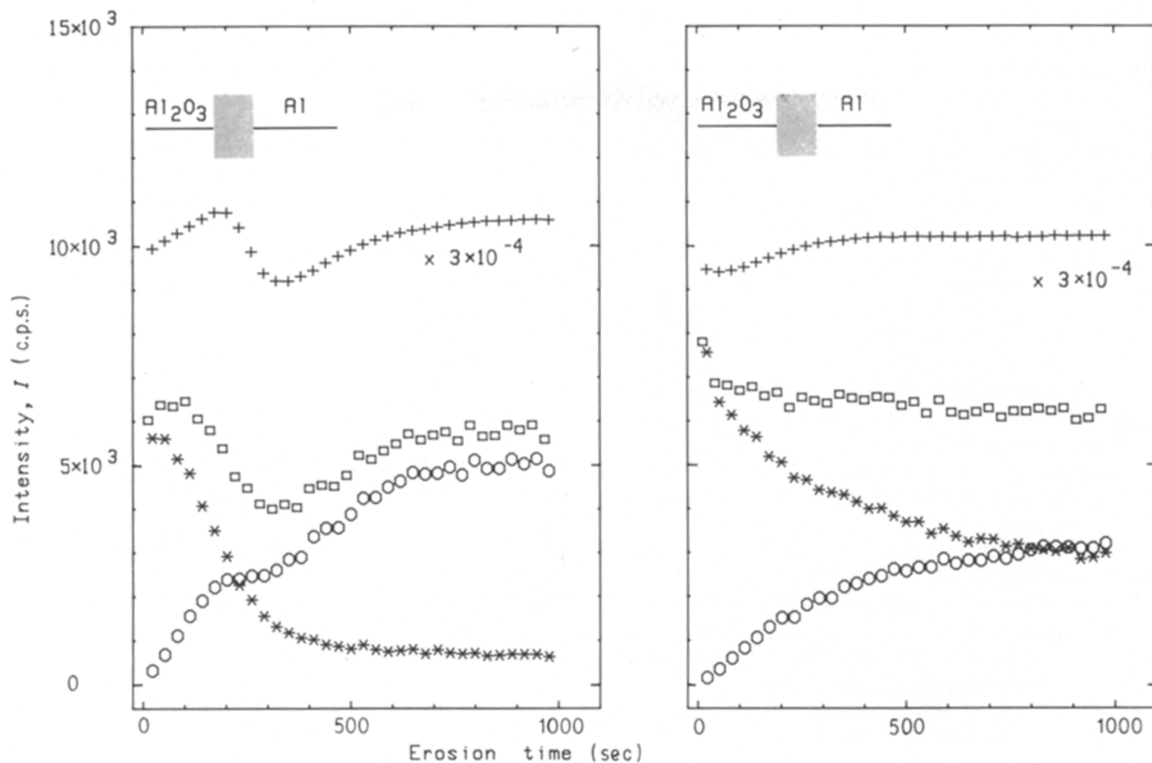

Figure 36 Depth profiles of the major and implanted elements for an aluminiun sheet covered by a 4.2 ± 0.5 nm oxide layer. (a) $^{18}O_2^+$ bombardment at medium energy (8 keV), (b) influence of $^{16}O_2$ flooding [32]. (+) $^{27}Al^+$, (*) $^{16}O^+$, (○) $^{18}O^+$, (□) $^{16}O^+$ + $^{18}O^+$.

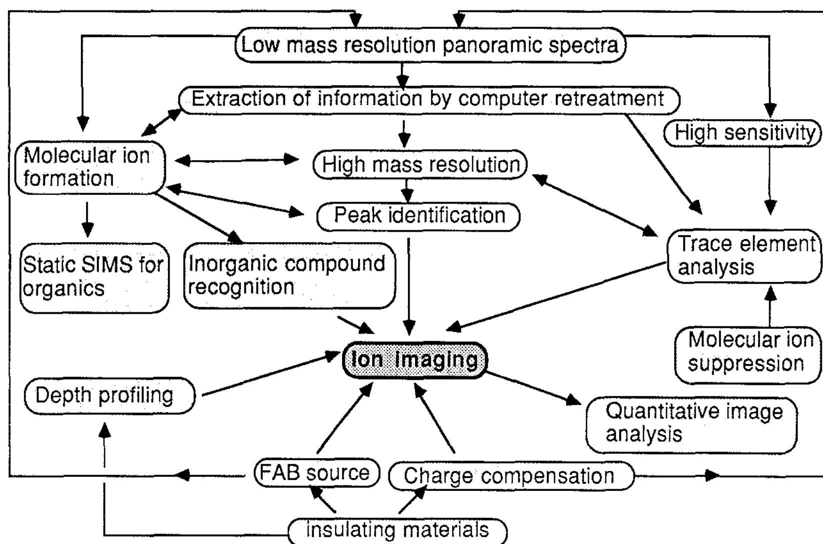

Figure 37 Schematic illustration of the major SIMS operating modes as used in materials science, illustrating their diversity and complementarity [69].

References

1. F. DEGRÈVE and J. M. LANG, in Proceedings of SIMS V Conference (Springer, Berlin, 1986) p. 388.
2. F. DEGRÈVE, N. A. THORNE and J. M. LANG, *Z. Anal. Chem.* **329** (1987) 410.
3. G. DEMORTIER (ed.), Proceedings of the 2nd International Conference on Chemical Analysis, Namur, September 1982 (North-Holland, 1982) p. 197.
4. G. L. KELLOG and T. T. TSONG, *J. Appl. Phys.* **51** (1980) 1184.
5. R. WAGNER, "Field Ion Microscopy" (Springer, Berlin, 1982).
6. A. W. CZENDERNA (ed.), "Methods of Surface Science Analysis" (Elsevier, Amsterdam, 1975).
7. G. BINNING, H. ROHER, Ch GERBER and E. WEIBEL, *Appl. Phys. Lett.* **40** (1982) 2178.
8. G. H. MORRISON and G. SLODZIAN, *Anal. Chem.* **47** (1975) 932A.
9. A. BENNINGHOVEN, F. G. RUDENAUER and H. W. WERNER, "Secondary Ion Mass Spectrometry" (Wiley, New York, 1987).
10. C. BRUNNÉE, *Int. Mass Spectrom. Ion Phys.* **76** (1987) 125.
11. H. W. WERNER, H. A. M. DE GREFT and J. Van den BERG, *Radd. Eff.* **18** (1974) 305.
12. H. W. WERNER and N. WARMOLTZ, *J. Vac. Sci. Technol.* **A2(2)** (1982) 726.
13. G. SLODZIAN, M. CHAINTREAU and R. DENNEBOUY, in Proceedings of SIMS V Conference (Springer, Berlin, 1986) p. 158.
14. G. BROCHARDT, S. SCHERRER and S. WEBER, *Mikrochim Acta* **2** (1981) 421.
15. F. DEGRÈVE and J. M. LANG, *Surf. Interface. Anal.* **7** (1985) 177.
16. A. BENNINGHOVEN, *Z. Phys.* **230** (1970) 403.
17. *Idem, CRC Crit. Rev. Solid State Sci.* **6** (1976) 291.
18. D. BRIGGS, *J. Vac. Sci. Technol.* **A2(2)** (1984) 1117.
19. G. BLAISE and M. BERNHEIM, *Surf. Sci.* **47** (1975) 324.

20. J. M. LANG and F. DEGRÈVE, *Surf. Interface Anal.* **7** (1985) 53.
21. C. A. ANDERSEN, in "Microprobe Analysis", edited by C. A. Andersen (Wiley, New York, 1973) p. 531.
22. G. SLODZIAN, in "Applied Charge Particle Optics", Advances in Electronics and Electron Optics, Suppl. 13B edited by A. Septier (Academic, New York, 1980) p. 1.
23. N. A. THORNE, A. DUBUS and F. DEGRÈVE, "Scanning Electron Microscopy IV (1986) p. 1255.
24. M. T. BERNIUS, Y. CH. LING and G. MORRISON, *Anal. Chem.* **58** (1986) 94.
25. R. W. ODOM, B. K. FURMAN, C. A. EVANS Jr, C. E. BRYSON, W. A. PETERSEN, M. A. KELLY and D. A. WAYNE, *ibid.* **55** (1983) 578.
26. J. M. GOURGOUT, in Proceedings of SIMS II Conference (Springer, Berlin, 1979) p. 286.
27. H. LIEBL, *Scanning* **3** (1980) p. 79.
28. R. LEVI-SETTI, G. CROWN and Y. L. WANG, in Proceedings of SIMS V Conference (Springer, Berlin, 1986) p. 132.
29. H. GNASER, J. FLEISCHAUER and W. O. HOFER, *Appl. Phys.* **A37** (1985) 211.
30. H. OECHNSER, in Proceedings of SIMS V Conference (Springer, Berlin, 1986) p. 70.
31. G. H. BECKER and K. T. GILLEN, in Proceedings of SIMS V Conference (Springer, Berlin, 1986) p. 85.
32. F. DEGRÈVE and J. M. LANG, in "Applied Materials Characterization Symposium", Vol. 48 (Materials Research Society, 1986) p. 241.
33. R. NAMDAR, *J. Microsc. Spectrosc. Electron.* **2** (1977) 293.
34. P. WILHARTITZ and M. GRASSERBAUER, *Mikrochim. Acta* **2** (1986) 313.
35. N. A. THORNE and F. DEGRÈVE, *Surf. Interface Anal,* **11** (4) (1988).
36. B. DUBOST, J. M. LANG and F. DEGRÈVE, in Proceedings of 3rd International Al–Li Conference, Oxford, UK, 1985 (Institute of Metals, London, 1986) p. 355.
37. P. WILLIAMS, C. A. EVANS Jr, M. L. GROSSBECK and H. K. BIRNBAUM, *Anal. Chem.* **48** (1976) 964.
38. M. L. GROSSBECK, P. WILLIAMS, C. A. EVANS Jr and H. K. BIRNBAUM, *Phys. Status Solidi* **34** (1976) k97.
39. T. OHSTUBO and K. SUZUKI, in Proceedings of SIMS IV Conference (Springer, Berlin, 1984) p. 426.
40. J. D. FASSETT and G. H. MORRISON, *Anal. Chem.* **50** (1978) 1861.
41. F. DEGRÈVE, *J. Microsc. Spectrosc. Electron.* **6** (1981) 223.
42. "Equilibrium Diagram of Aluminium Alloys Systems" (Aluminium Development Association, London 1961) p. 95.
43. D. E. NEWBURY and D. SIMONS, in Proceedings of SIMS IV Conference (Springer, Berlin, 1984) p. 101.
44. B. K. FURMAN and G. H. MORRISON, *Anal. Chem.* **52** (1980) 2305.
45. F. DEGRÈVE, J. M. LANG, F. BODART and G. DEMORTIER, Poster presented at the AFSM Meeting, April 1986, Grenoble.
46. N. A. THORNE, A. DUBUS, J. M. LANG and Ph. MEYER, in Proceedings of 4th International Al–Li Conference, Paris, 1987, Vol. 48 (Editions de Physique, Les Ullis, 1987) p. C3-521.
47. F. DEGRÈVE, B. DUBOST, A. DUBUS, N. A. THORNE, F. BODART and G. DEMORTIER, in Proceedings of 4th International Conference, Paris, 1987, Vol. 48 (Editions de Physique, Les Ullis, 1987) p. C3-505.
48. J. C. PIVIN, C. ROQUES-CARMES and G. SLODZIAN, *Appl. Phys.* **51**(8) (1980) 4158.
49. R. NAMDAR, D. LOISON and R. TIXIER, *J. Phys. C2.* **45** (1984) 673.
50. L. HABRAKEN, T. D. SHUNGU and V. LEROY, *Le Vide, Couches Minces* (1979) 199.
51. J. C. JOUD, R. FAURE, R. NAMDAR, C. PICHARD and P. POYET, *Mém. Et. Sci. Rev. Métal.* (1982) 235.
52. M. TEXTOR and R. GRAUER, *Corros. Sci.* **23** (1983) 71.
53. J. C. PIVIN and D. LOISON, *J. Phys. C2* **45** (1984) 647.
54. R. C. FURNEAUX, G. E. THOMPSON and G. C. WOOD, *Corros. Sci.* **18** (1978) 853.
55. W. GUST, C. OSTERTAG, A. LODDING, B. PEDEL and H. ODELIUS, *Phil. Mag.* **47** (1983) 395.
56. M. P. MACHT and V. NAUNDORF, *J. Appl. Phys.* **63** (11) (1982) 7551.
57. L. LALINOWSKI and R. SEGUIN, *Appl. Phys. Lett.* **35** (1979) 211.
58. F. DEGRÈVE, S. DEMARKAR and A. DUBUS, *J. Microsc. Spectrosc. Electron* **7** (1982) 243.
59. T. F. BOWER, H. D. BRODY and M. C. FLEMINGS, *Trans. Met. Soc. AIME* **236** (1966) 624.
60. S. R. BRYAN, R. W. LINTON and D. P. GRIFFIS,in Proceedings of SIMS V Conference (Springer, Berlin, 1986) p. 235.
61. E. D. HONDROS and M. P. SEAH, *Int. Metal. Rev.* No. 222 (Dec. 1977) 262.
62. J. M. LANG, F. DEGRÈVE and N. A. THORNE, 4th International Al–Li Conference, Paris, 1987 Vol. 48 (Editions de Physique, Les Ullis, 1987) p. C3-693.
63. W. GUST, M. B. HINTZ, A. LODDING, H. ODELIUS and B. PEDEL, *Acta. Metall.* **28** (1980) 291.
64. J. C. PIVIN, D. LOISON, C. ROQUES-CARMES, J. CHAUMONT, A. M. HUBER and G. MORILLOT, in Proceedings of SIMS III Conference (Springer, Berlin, 1982) p. 274.
65. D. LOISON, J. C. PIVIN, J. CHAUMONT and C. ROQUES-CARMES, *Nucl. Instrum. Meth.* **209/210** (1983) 975.
66. J. C. MIKKELSEN Jr, *J. Electron Mater.* **11** (1983) 541.
67. C. A. EVANS Jr and P. P. PEMSLER, *Anal. Chem.* **42** (1970) 1060.
68. M. J. GRAHAM, in Proceedings of the International Corrosion Congress, Toronto, May 1984, p. 1.
69. N. A. THORNE and F. DEGRÈVE, in Proceedings of SIMS VI Conference, Versailles, France, Sept. 1987, in press.

Received 11 August 1986
and accepted 17 December 1987